CrossMark

JM PAPERS

Combined three-dimensional flow field measurements and motion tracking of freely moving spheres in a turbulent boundary layer

R. van Hout[1],†, A. Hershkovitz[1], G.E. Elsinga[2] and J. Westerweel[2]

[1]Faculty of Mechanical Engineering, Technion – Israel Institute of Technology, Technion City, Haifa 32000, Israel

[2]TU-Delft, 3ME Aero- and Hydrodynamics Laboratory, Leeghwaterstraat 21, 2628CA Delft, The Netherlands

A combination of time-resolved tomographic particle image velocimetry, refractive index matching technique and machine vision algorithms was used to measure the translational and rotational motion of freely moving, nearly neutrally buoyant spheres in a fully developed turbulent boundary layer (TBL). Located in the buffer and logarithmic layers, the hydrogel spheres ($\sim$70 inner wall units in diameter) were refractive index matched with the water and tagged by 'spokes'. Besides translational motion, the spheres exhibited significant rotation. The spheres were surrounded by typical coherent structures observed in TBLs, among them hairpin packets and transverse and longitudinal vortices that induced ejections and sweeps. While the majority of instantaneous sphere Reynolds numbers did not exceed 100, and vortex shedding was not observed, the results showed that the spheres may affect the evolution of hairpin packets in TBLs due to their finite size. The instantaneous rotation-, wall- and shear-induced lift forces, as well as the drag forces, acting on the spheres were estimated using available correlations for the lift and drag coefficients. Results hinted at negative shear-induced lift due to flow separation at a smaller critical Reynolds number than incorporated in the correlations that do not include the effect of ambient turbulence. The results indicated further that the drag force aided by the rotation-induced lift force was instrumental in keeping one of the spheres aloft. For the wall-ward moving spheres, lift forces opposed sphere motion. As a result, the spheres approached the wall with velocities lower than their quiescent settling velocity.

Key words: particle/fluid flow

† Email address for correspondence: rene@technion.ac.il

944 A12-1

1. Introduction

Particle transport plays a key role in many natural and industrial settings, for example in the advection of deep sea microplastics (Kane & Clare 2019), as well as in the transport of particulates by pneumatic or hydraulic conveyors used in the food, chemical and pharmaceutical industries (Woodcock & Mason 1987). Understanding the physical mechanisms that control particle transport is therefore of the utmost importance from a basic scientific perspective as well as for developing practical applications.

In turbulent flows, particle deposition, lift-off and re-entrainment take place in the vicinity of walls where particles interact with a turbulent boundary layer (TBL) (Mollinger & Nieuwstadt 1996; Muthanna, Nieuwstadt & Hunt 2005; van Hout 2013). The main forces that govern particle motion are gravitation, buoyancy, drag and lift forces, the latter acting perpendicular to the drag. In case strong accelerations are present, inertial forces such as the added mass force and the Basset (history) force may be of importance (Maxey & Riley 1983), and when particle surface interactions occur, friction and electrostatic forces need to be considered (Minier & Pozorski 2017).

Traditionally, particle lift-off has been treated as a threshold phenomenon based on the balance between mean gravitational, buoyancy and drag forces (Bagnold 1951). However, particle transport, much like momentum and heat transfer, is associated with intermittent TBL motions due to ejection–sweep cycles (termed 'turbulent bursts'; Sutherland 1967). During recent decades, many numerical and experimental investigations have provided evidence for the importance of ejection–sweep cycles in particle deposition and re-suspension. Early experiments used cinematography to track particles (Sumer & Oguz 1978; Sumer & Deigaard 1981; Rashidi, Hetsroni & Banerjee 1990; Niño & Garcia 1996), while in the last decade (combined) particle image velocimetry (PIV) and particle tracking velocimetry (PTV) studies (van Hout 2011, 2013; Rabencov, Arca & van Hout 2014; Rabencov & van Hout 2015; Ebrahimian, Sanders & Ghaemi 2019; Ahmadi, Sanders & Ghaemi 2020; Baker & Coletti 2021) have enabled us to resolve the three-dimensional (3-D) particle–flow interaction at high Reynolds numbers, thereby surpassing current numerical capabilities. The latter suffer from high computational cost, usually alleviated by employing modelling assumptions such as the 'point-particle' approach (Balachandar & Eaton 2010). Based on statistical techniques such as quadrant analysis (Niño & Garcia 1996; Soldati & Marchioli 2009; van Hout 2011; Ahmadi *et al.* 2020; Baker & Coletti 2021) as well as tracking the motion of only a few spheres (Sumer & Oguz 1978; Sumer & Deigaard 1981; van Hout 2013), it has become clear that spherical particles are lifted off the wall mainly by intense ejections often in combination with sweeps (van Hout 2013).

Comprehensive measurements by Niño & Garcia (1996) showed that near-wall particle motion was dominated by quasi-streamwise vortices that generated so-called low- and high-speed streaks. Particles immersed within the viscous sublayer segregated preferentially in the low-speed streaks, in contrast to larger particles that did not segregate preferentially. They showed that particles were lifted off the wall by ejections at angles between $10°$ and $20°$, in agreement with Sutherland (1967). Rashidi *et al.* (1990) investigated size-driven effects further, and showed that small- and large-diameter polystyrene spheres decreased and increased the number of ejection events, respectively. In addition, increased particle loading enhanced size-driven effects without changing the burst frequency and the mean low-speed streak spacing.

During the last decade, increasingly sophisticated experimental techniques have enabled the simultaneous measurement of bead and fluid velocities (van Hout 2013; Ebrahimian *et al.* 2019; Ahmadi *et al.* 2020; Baker & Coletti 2021). For example, van Hout (2011, 2013) used combined planar PIV-PTV to resolve spatially and temporally the motion of polystyrene beads as well as the surrounding water velocities in a TBL. He identified three lift-off trajectories: (i) slow ascent, (ii) steep ascent, and (iii) saltation. The specific trajectory shape depended on the sequence and type of coherent turbulent structures encountered by the beads during their ascent. Bead lift-off was synchronized with a sharp peak in the shear-induced lift force, while the wall-normal drag force opposed the lift force as the beads gained height. Using the same data processing procedure as developed by van Hout, Sabban & Cohen (2013), Baker & Coletti (2021) performed a comprehensive statistical analysis of polystyrene bead interaction with a TBL, and in particular provided information on bead accelerations. Employing state-of-the-art time-resolved tomographic PIV-PTV, Ahmadi *et al.* (2020) and Ebrahimian *et al.* (2019) investigated the 3-D particle–flow interaction of polystyrene and glass beads in a turbulent channel flow. Based on bead acceleration, Ebrahimian *et al.* (2019) identified an inner layer (comprising the viscous sublayer and part of the buffer layer) where beads decelerated and accelerated in the streamwise and wall-normal directions, respectively. In the outer layer, beads accelerated in the streamwise direction with maximum momentum transfer in the logarithmic layer. In addition, Ebrahimian *et al.* (2019) showed that bead–wall interaction depended on incident angles, and that assuming point-particles and elastic particle–wall collisions is inadequate to model accurately large inertial beads in turbulent wall-bounded flows. Bead rotation was not measured in the above-discussed studies.

As mentioned previously, the majority of numerical studies use the point-particle approach (Balachandar & Eaton 2010) in which finite-size effects and particle rotation are not accounted for. However, in recent years, particle-resolved simulations (Zhao & Andersson 2011; Ardekani & Brandt 2019; Peng, Ayala & Wang 2019; Yousefi, Costa & Brandt 2020) have indicated that particle rotation leads to turbulence modulation and should not be neglected. The simultaneous measurement of the 3-D flow field and the motion (translation and rotation) of a freely moving particle is challenging (Bellani *et al.* 2012; Klein *et al.* 2012). Recently, using stereoscopic imaging, Tee, Barros & Longmire (2020) measured the translation as well as rotation of individual finite-sized magnetic wax spheres released in a TBL. Small markers on the sphere's surface allowed tracking. Besides sphere saltation, re-suspension and sliding on the wall, also spanwise sphere translation was observed, suggesting that spanwise forces are important. Repeated sphere lift-off events of forward rolling spheres were attributed to the Magnus lift force. They did not capture simultaneously the instantaneous velocity in the vicinity of the spheres.

The present research is motivated by the lack of detailed quantitative information on the coupled 3-D rotational and translational dynamics of a freely moving sphere and the surrounding flow field in a TBL flow. The novelty of the present work lies in the simultaneous measurement of sphere and flow dynamics using a combination of time-resolved tomographic particle image velocimetry (tomo-PIV) and refractive index matched hydrogel spheres. The spheres were tagged by tracer particles such that their rotational as well as translational motion could be determined. The finite-sized spheres had diameters of approximately 70 inner wall units, invalidating the point-particle approach. The experimental set-up and data processing are described in § 2. Results on translational and rotational sphere dynamics, and their interaction with the coherent structures found

in TBLs, are presented in § 3, including a discussion of the forces acting on the spheres. Finally, a short discussion and summary are presented in § 4.

2. Experimental set-up and data processing

2.1. *Experimental set-up*

The measurements were performed in the closed-loop water flume at the Laboratory for Aero- and Hydrodynamics at Delft University of Technology. The cross-section of the water volume that filled the flume at the measurement position was $61.6 \times 61 \, \text{cm}^2$ (width × height). The experiments were performed 4 m downstream of the entrance to the channel. In order to ensure a fully developed TBL at the measurement position, a zigzag trip (Elsinga & Westerweel 2011) was placed 500 mm downstream of the test section inlet to force transition to turbulence. A false bottom (2.5 cm thick) was positioned 16.5 cm above the actual bottom of the channel, on top of two elongated, rectangular supports, as depicted in figure 1. The 'effective' (open) flow area was $A_e = 0.3521 \, \text{m}^2$. The streamwise, wall-normal and transverse directions are denoted x_1, x_2 and x_3, respectively (figure 1), and corresponding instantaneous flow velocities are denoted U_i ($i = 1, 2, 3$). The origin of the coordinate system was positioned on the false bottom wall at the start of the volume of interest (VOI) in the streamwise direction and at the edge of the VOI in the spanwise direction (see inset in figure 1*d*). Here and in the following, temporal and spatial averages are denoted by an overbar and angle brackets, respectively. Normalization by inner wall parameters – i.e. by the friction velocity u_τ and the kinematic water viscosity ν – is denoted by the superscript '+'. Fluctuating velocity components were calculated by Reynolds decomposition, $U_i = \bar{U}_i + u_i$, where u_i ($i = 1, 2, 3$) denote the instantaneous fluctuating velocity components. Root-mean-square (r.m.s.) values are indicated by a prime.

A frequency-controlled pump was used to circulate the water through the closed-loop water flume. The bulk flow velocity based on A_e was $U_b = 0.174 \pm 0.002 \, \text{m s}^{-1}$, and the corresponding bulk Reynolds number was $Re = U_b h / \nu = 7.3 \times 10^4$, where h ($= 420 \, \text{mm}$) is the water level measured from the false bottom upwards, and ν was taken at the measured water temperature ($T = 27 \, ^\circ\text{C}$).

The experiments were performed using a tomo-PIV set-up consisting of four high-speed cameras (Imager Pro HC, 2016×2016 pixels), a high-speed laser (Nd:YLF, Darwin Duo 80M, Quantronix), optics, and acquisition/processing software (LaVision GmbH). Near-neutrally buoyant hollow glass spheres ($\sim 10 \, \mu\text{m}$, Sphericell, Potter's Industries) were used as tracer particles. This set-up allowed us to measure all three instantaneous flow components in a volumetric domain (Adrian 2011).

The cameras were mounted on a rigid frame that was not connected to the water channel to minimize vibrations, and their set-up is displayed schematically in figures 1(*b–d*). Cameras 1 and 2 were level with the false bottom, with viewing angles about the x_1–x_3 plane of 24° and 29°, respectively, while cameras 3 and 4 viewed the VOI from above as depicted schematically in figures 1(*c,d*). Note that no prisms were used to reduce refraction, and as a result, the effective solid angle of the camera set-up was less than depicted. All cameras were equipped with lenses (micro-Nikkor, Nikon) mounted on Scheimpflug adapters to ensure focus across the cameras' fields of view. The focal lengths of the lenses were 105 mm (cameras 1 and 2, f-numbers $f^\# = 16$) and 200 mm (cameras 3 and 4, $f^\# = 22$). Note that the f-numbers of the lenses were set high enough to ensure sufficient depth of focus across the illuminated VOI.
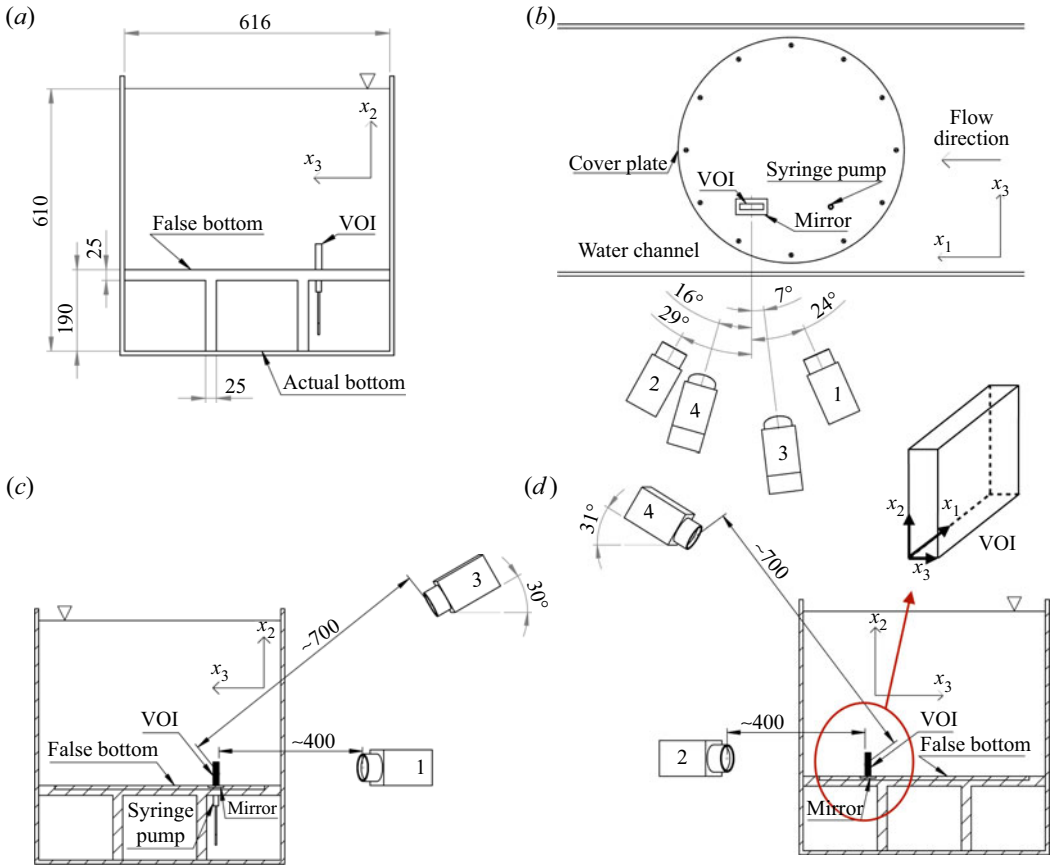
944 A12-4

Figure 1. Schematic layout of the experimental set-up: (*a*) cross-section of the flume at the measurement position. Tomo-PIV camera set-up: (*b*) top view, and side views of cameras (*c*) 1 and 3, (*d*) 2 and 4. All dimensions are in mm. Inset in (*d*) shows the origin of the employed right-handed coordinate system.

The laser beam was expanded and collimated using two cylindrical lenses and passed through a knife-edge filter to ensure well-defined edges of the VOI in the x_3-direction. It was guided to enter the flume from the top, and a stationary water-filled acrylic hydrodynamically shaped 'box' was used to remove any surface waves. The dimensions of the VOI were approximately $60 \times 60 \times 15 \, \text{mm}^3$ (length × height × width). In order to ensure sufficient light intensity, a mirror was placed within the false bottom (under a cover plate) in order to reflect the expanded and collimated laser beam back to the VOI.

To obtain visual access around the freely moving sphere with a limited number of cameras, refractive index matched hydrogel spheres were used (see also Bellani *et al.* 2012; Klein *et al.* 2012). These were bought in dry state (∼2 mm in diameter), and after they were soaked in water for a few minutes, they attained diameters between 7 and 8 mm. Despite their large water content, the hydrogel spheres were not neutrally buoyant, and their material density was determined based on settling velocity measurements in a 1.5 m high, quiescent water column (diameter 9 cm). The density of the spheres when fully saturated was $\rho_s = 1002 \pm 0.3 \, \text{kg m}^{-3}$. In order to determine the spheres' translational and rotational movement, tracer particles were injected into the hydrogel spheres, leaving four to five 'spokes' inside them. Figure 2(*a*) shows an example of a hydrogel sphere imaged
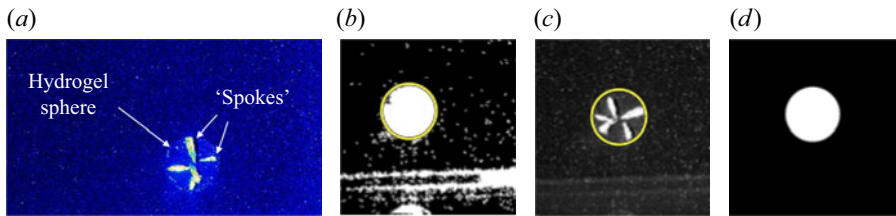
(*a*)   (*b*)   (*c*)   (*d*)

Figure 2. Overview of the sphere detection procedure. Cropped images (single camera) of: (*a*) raw PIV data showing the spokes imaged within the hydrogel sphere and the tracer particles in its vicinity; (*b*) silhouette enhanced (and 'holes' filled) sphere. The sphere's perimeter was detected using the circular Hough transform and is indicated by a yellow circle in (*b,c*). (*c*) Detected sphere perimeter containing the 'spokes'. (*d*) Generated binary mask.

by one of the cameras during the experiment. Several spheres with 'spokes' were prepared prior to the experiments and placed inside a 5 ml syringe having inner diameter 11 mm. The syringe was flush-mounted with the top of the false bottom, and positioned 20 cm upstream of the VOI (figure 1*b*). It was driven manually by a second syringe that was located outside the flume. During an experiment, spheres were slowly, one by one, released into the TBL. One data set (3140 images) was acquired for the undisturbed boundary layer flow (without spheres), and four additional data sets including freely moving spheres were acquired at acquisition frequency 250 Hz to ensure time series conditions. Although several spheres would traverse the VOI during a single set, only one single sphere would be present at a certain time instant. In addition, in order for the data processing algorithm (discussed in the next subsection) to work, the spokes had to be well imaged while the spheres had to reside within the VOI for the most part of their passage through the VOI. In total, four different spheres that satisfied these requirements were tracked and processed, as will be discussed below.

2.2. *Data processing*

2.2.1. *Undisturbed boundary layer flow*

Data processing was different for the undisturbed boundary layer flow and the data sets containing the freely moving spheres. The former were processed using 'standard' tomo-PIV data processing procedures similar to those described by van Hout *et al.* (2018). These comprised image pre-processing, self-calibration, tomographic reconstruction of the 3-D light intensity field, and direct correlation to obtain the 3-D velocity vector fields (Elsinga *et al.* 2006). The 3-D intensity field was reconstructed using the fast multiplicative algebraic reconstruction technique (fast MART) algorithm as implemented in DaVis 8.2 (LaVision GmbH) using six iterations. The transverse borders of the VOI were based on the mean reconstructed intensity field and were taken as the locations where the signal-to-noise ratio exceeded 3. The resulting VOI width was 15 mm, matching the width set by the knife-edge filter. The position of the wall was determined by the location of a sharp peak in mean intensity as a result of reflections at the wall.

The 3-D velocity vector fields were determined by direct cross-correlation using a multi-pass approach (van Hout *et al.* 2018) having final interrogation volumes $40 \times 40 \times 40$ voxels at 75 % overlap, leading to a vector spacing of 0.23 mm corresponding to 2.1 inner wall units. Note that the spatial measurement resolution is dictated by the interrogation volume size, which corresponds to 8.4 inner wall units. Post-processing

944 A12-6

of the vector maps comprised (i) universal outlier detection, (ii) 'fill' removed data by interpolation, and (iii) smoothing. In order to further reduce noise, second-order polynomial regression (Elsinga *et al.* 2010) was applied to the vector maps, and velocity derivatives were based on the least-squares fitted polynomials. Data quality was validated by evaluating the continuity equation, and typical values of the coefficient of determination in the centre part of the VOI were $R^2 \approx 0.7$, i.e. similar to those reported by van Hout *et al.* (2018).

Based on the undisturbed boundary layer data, the friction velocity u_τ was determined using the Clauser method (Clauser 1956), taking the von Kármán constant and intercept value as $\kappa = 0.41$ and $B = 5.0$ (Schlichting & Gersten 2000), respectively.

2.2.2. *Data sets containing the sphere*

Sequences of raw PIV images were pre-processed to enhance the sphere's silhouette, which could be distinguished from the background PIV image despite the refractive index matching technique that was employed (figure 2). The resulting greyscale images were binarized, small-scale noise was removed by a two-dimensional (2-D) median filter, and subsequently 'holes' were filled (figure 2*b*). The enhanced sphere's silhouette was detected using the circular Hough transform (figures 2*b,c*; Pedersen 2007), and a mask was generated for each camera and image in the sequence (figure 2*d*). Based on these 2-D masks, a visual hull of the sphere was reconstructed in space (van Hout *et al.* 2018) and converted into a point-cloud. Its geometric centre was calculated and used as an estimate of the sphere's position in space, while the diameter of the largest sphere confined within the boundaries of the visual hull was used as an estimate of the sphere's diameter. The uncertainty of the estimated sphere position did not exceed 0.15 mm in each direction, i.e. less than 2 % of the typical sphere diameter.

The determined diameter and centre position of the sphere were used to separate the spokes from the surrounding tracer particles so that they could be processed separately. An example of the 3-D sphere volume containing the spokes as well as single tracer particles near the sphere's boundary is shown in figure 3. In order to determine the sphere's translation and rotation, several methods were considered based on: (i) direct cross-correlation, (ii) 3-D line detection using the 3-D Hough transform (Dalitz, Schramke & Jeltsch 2017); and (iii) the iterative closest point (ICP) algorithm (Smistad *et al.* 2015). The first method was too time-consuming, while the second proved unreliable due to the spokes' irregular shapes. The employed ICP algorithm (Smistad *et al.* 2015) determines the rigid body transformation between two point-clouds (source and target) by approximating the best-fitted (least-squares) transformation through iteratively matching each point in the source to its nearest neighbour in the target. In order to apply this method, the masked reconstructed sphere volumes were converted to 'sparse' point-clouds, and as an initial guess, the sphere centre displacement was based on its estimated centroid positions to increase accuracy and speed up convergence. Besides the sphere displacement, this method also provided the sphere's change in orientation about x_1, x_2 and x_3, i.e. $\Delta\alpha_1$ (roll), $\Delta\alpha_2$ (pitch) and $\Delta\alpha_3$ (yaw), respectively. Based on the determined change in orientation, instantaneous angular velocities were determined by $\dot{\alpha}_i = \Delta\alpha_i/\Delta t$ ($i = 1, 2, 3$) in rad s^{-1}, where Δt is the time difference between subsequent frames. The quality and accuracy of point-cloud registration using ICP is given by the r.m.s. error. Typical values of the r.m.s. error were 2–3 pixels, i.e. 0.06–0.1 mm. Assuming that all errors are purely translational or rotational, typical uncertainties of the spheres' displacement and change in orientation
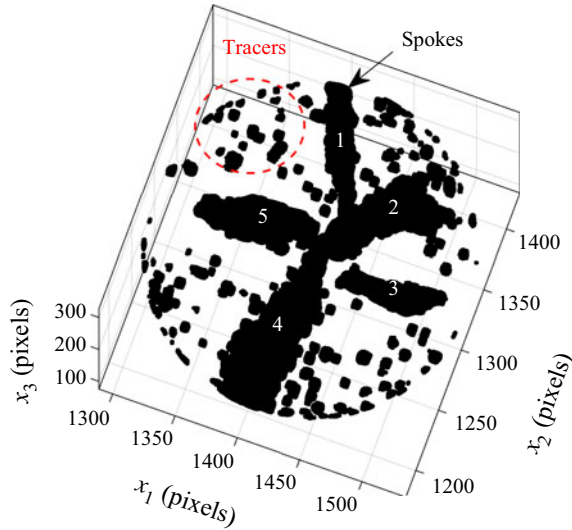
Figure 3. Example of the binarized reconstructed light intensity field confined within the determined sphere boundary. Spokes are numbered from 1 to 5. Tracer particles at the perimeter of the sphere are shown as small black dots (examples within dashed red ellipse).

were smaller than 1.5 pixels (0.05 mm) and 0.01 rad in each direction, respectively. Note that these are conservative estimates and that the actual uncertainties are expected to be lower. Instantaneous streamwise, wall-normal and transverse sphere centroid velocities and sphere angular velocities are denoted by V_i and $\dot{\alpha}_i$ ($i = 1, 2, 3$), respectively. Sphere centroid positions are indicated by $x_{i,c}$ ($i = 1, 2, 3$), where the subscript 'c' denotes the sphere centroid position.

Tracks of sphere centroid positions as well as their translational and angular velocities were smoothed to reduce random noise by applying robust local regression with weighted linear least-squares and a second-degree polynomial model (Cleveland 1979; 'rloess' as implemented in Matlab). In order to limit filtering of relevant data, the span of the local regression was based on a four-point stencil preceding and succeeding each data point, corresponding to $\Delta t = 32$ ms, i.e. approximately twice the sphere's response time, $\tau_s = (\rho_s - \rho)D^2/18\mu \approx 15.3$ ms, where ρ denotes the water density (at 27 °C) and μ denotes the dynamic water viscosity (at 27 °C). Note that this sphere's response time, which is used commonly in particle-laden flows (e.g. Ebrahimian *et al.* 2019; Baker & Coletti 2021), is derived from a force balance on a sphere settling in a quiescent fluid assuming Stokes drag. This definition is used commonly when ($\rho_s - \rho$) is small, and for neutrally buoyant small particles would lead to a zero response time (i.e. flow tracers). The Kolmogorov time scale τ_k at $x_2^+ \approx 100$ was estimated to be $\tau_k \approx 79$ ms (see § 3.2.1), i.e. twice the span of the local regression and approximately $5\tau_s$, indicating that the sphere response time and span of the regression are small with respect to the smallest turbulence scales. Uncertainties in sphere position and time step Δt^+ were estimated as $\delta x_{i,c}^+ = 1$ and $\delta(\Delta t^+) = 0.07$, respectively. Based on the smoothed centroid positions, components of the translational sphere centroid velocity vectors were calculated by two methods: (i) a central difference scheme using forward and backward differences at the start and end of the trajectories; and (ii) taking the derivative of a locally least-squares fitted second-order polynomial.

944 A12-8

After determining the 3-D sphere centroid positions, the sphere volumes were masked in the 3-D reconstructed intensity fields, after which the 3-D flow field around the spheres was calculated by tomo-PIV data processing similarly as discussed in § 2.2.1. Note that the spatial resolution of the tomo-PIV (see § 2.2.1) was insufficient to resolve the boundary layer on the sphere. In studying particle-laden flows, it is important to know the particle's motion relative to the flow velocity evaluated at the particle's position characterized by the instantaneous relative velocity vector (here, vectors are denoted in bold typeface) between the sphere and the fluid $U_r = V - U_c$. Here, V is the sphere velocity vector (based on the derivative of the locally fitted second-order polynomial), and U_c is the 'undisturbed' instantaneous water velocity vector at the sphere's centroid position, as indicated by the subscript 'c'. Note that in an experiment, the 'undisturbed' fluid velocity cannot be determined since the presence of the spheres disturbs the flow in its vicinity. Bearing this in mind, a practical approach was taken and U_c was determined by interpolation techniques (see also van Hout 2013; Baker & Coletti 2021). Here, water velocity vectors at the sphere's centroid position were determined using a robust iterative method for 3-D data gap-filling (Garcia 2010). The accuracy of this method was tested on a data set without sphere for which the 3-D velocity field was known. We removed 3-D velocity vectors occupying a spherical volume the same size as the hydrogel sphere, and the 3-D data gap-filling method was used iteratively to interpolate the 3-D velocity field. R.m.s. values of the differences between the interpolated and the original 3-D velocity field were comparable to typical uncertainties of an instantaneous PIV measurement (0.1–0.2 pixels; Wieneke 2008). The water velocity vector at the position of the sphere centroid, U_c, was evaluated by two methods: (i) as the interpolated velocity at the sphere centroid (indicated by the superscript 'c'); and (ii) as the velocity vector averaged spatially over all interpolated water velocities confined within the sphere volume ('volume averaged', denoted by superscript 'v').

3. Results

3.1. *Undisturbed turbulent boundary layer*

The wall-normal profile of the temporally and spatially averaged, normalized streamwise velocity $\langle \bar{U}_1 \rangle^+$ is depicted in figure 4 together with the 'theoretical' velocity profiles in the viscous sublayer, $U_1^+ = x_2^+$, and in the log layer, $U_1^+ = (1/\kappa) \ln x_2^+ + B$ ('log-law'; Pope 2000), where κ ($= 0.41$) denotes the von Kármán constant, and the intercept is $B = 5.0$. The spatial average was taken over the transverse and streamwise directions. In addition to the present data, laser Doppler velocimetry (LDV) measurements by De Graaff & Eaton (2000) are also plotted in figure 4. As can be seen, for $x_2^+ \geq 8$, the wall-normal profile of $\langle \bar{U}_1 \rangle^+$ matches closely the measurements by De Graaff & Eaton (2000) and log-law behaviour is observed for $30 \leq x_2^+ \leq 200$. Measurements by De Graaff & Eaton (2000) were performed at higher momentum thickness Reynolds numbers Re_θ, and as a result, the outer layer is shifted to larger x_2^+ values. Close to the wall ($x_2^+ < 8$), the tomo-PIV measurements deviate from the velocity profile in the viscous sublayer due to the finite size of the interrogation volume (van Hout *et al.* 2018) and the strong gradients near the wall.

The mean streamwise velocity at the edge of the boundary layer was estimated based on the plateau values that were reached farthest away from the wall, i.e. $U_e = 0.189 \pm 0.001 \text{ m s}^{-1}$ ($U_e/U_b = 1.086$). The boundary layer thickness $\delta = 43 \pm 3 \text{ mm}$ was determined as the wall-normal position for which $\langle \bar{U}_1 \rangle = 0.99 U_e$. Based on the measured
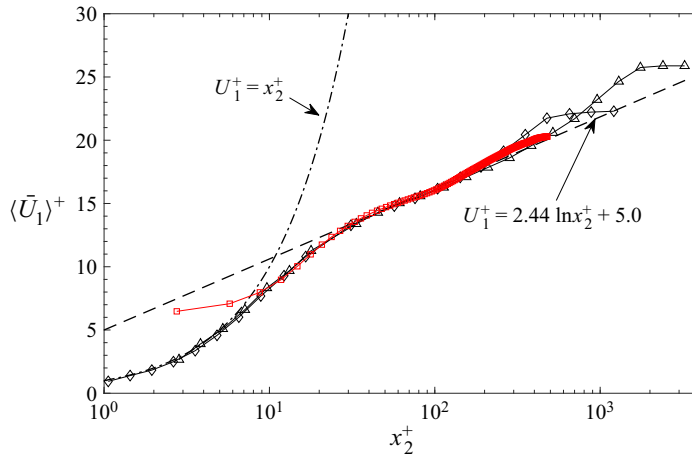
Figure 4. Semi-logarithmic plot of $\langle \bar{U}_1 \rangle^+$ as a function of x_2^+. Present data: red squares denote $Re_\theta = 850$; the dash-dot curve denotes the velocity profile in the viscous sublayer; the dashed line denotes the 'log-law'. Literature results (De Graaff & Eaton 2000): diamonds denote $Re_\theta = 1430$; triangles denote $Re_\theta = 5200$.

velocity profile, the displacement and momentum thicknesses were $\delta^* = 6.03 \pm 0.03$ mm and $\theta = 4.47 \pm 0.05$ mm, respectively, giving a shape factor $H = \delta^*/\theta = 1.35 \pm 0.01$, i.e. within the range of typical values for TBLs (Schlichting & Gersten 2000). The momentum thickness Reynolds number was $Re_\theta = U_e\theta/\nu = 850 \pm 10$. The friction velocity $u_\tau = 0.009 \pm 0.001 \, \mathrm{m\,s^{-1}}$ was determined by the Clauser method (Clauser 1956) assuming $\kappa = 0.41$ and $B = 5.0$, giving friction Reynolds number $Re_\tau = u_\tau \delta/\nu = 390 \pm 50$.

Wall normal profiles of the normalized and spatially averaged Reynolds stress components, $\langle \overline{u_1 u_1} \rangle^+$, $\langle \overline{u_2 u_2} \rangle^+$ and $-\langle \overline{u_1 u_2} \rangle^+$, are depicted in figure 5 and also compared to measurements by De Graaff & Eaton (2000) as well as hot-wire measurements by Erm & Joubert (1991) ($Re_\theta = 697$ and 1003). The present results compare well with those of Erm & Joubert (1991) and De Graaff & Eaton (2000). However, note that in the tomo-PIV measurements, the $\langle \overline{u_1 u_1} \rangle^+$ profile becomes governed by noise for $x_2^+ \leq 15$ (figure 5(a); see also van Hout *et al.* 2018).

The present data sets enable us to visualize the 3-D vortex structures residing in the TBL using the *Q*-criterion (Hunt, Wray & Moin 1988; van Hout *et al.* 2018). An example of a snapshot depicting vortical structures as *Q*-criterion iso-surfaces overlaid with the normalized streamwise and transverse vorticity, ω_1^+ and ω_3^+, is shown in figures 6(*a*) and 6(*b*), respectively, while a different viewing angle of the same snapshot is depicted in figure 7. This snapshot shows typical vortical structures residing in the TBL. Note that close to the wall ($x_2^+ \leq 15$), the data are noisy due to the limited spatial measurement resolution. The main vortices prominent in this snapshot are a pair of uplifted, unconnected counter-rotating vortices (denoted 'SV1' and 'SV2' in figures 6 and 7). The largest of the pair (SV2) exhibits a characteristic 'cane' shape (Robinson 1991). SV1 and SV2 are uplifted from the wall at an angle of approximately $40°$–$45°$, typical of hairpin structures (Adrian 2007). Note that due to the limited transverse extent of the VOI ($\Delta x_3^+ \approx 150$), our measurements do not reveal the complete structure of SV2, or any connection between SV1 and SV2. In addition, in the present data set, we did not observe fully developed, connected hairpin structures likely since typically, they have transverse widths of approximately 100–150 inner wall units (Adrian 2007), i.e. comparable to the width of the VOI.
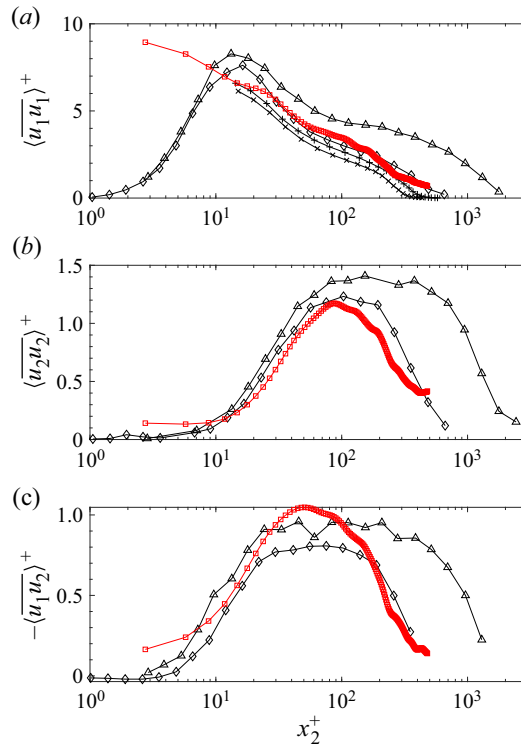
944 A12-10

Figure 5. Semi-logarithmic plots of the wall-normal profiles of the normalized Reynolds stress components: (a) $\langle \overline{u_1 u_1} \rangle^+$, (b) $\langle \overline{u_2 u_2} \rangle^+$, and (c) $-\langle \overline{u_1 u_2} \rangle^+$. Present data: red squares denote $Re_\theta = 850$. Literature results: from De Graaff & Eaton (2000), diamonds denote $Re_\theta = 1430$, and triangles denote $Re_\theta = 5200$; from Erm & Joubert (1991), $\times$ symbols denote $Re_\theta = 697$, and $+$ symbols denote $Re_\theta = 1003$.

Based on the proximity and similarity of SV1 and SV2, and the fact that they seem to comprise the 'legs' of a hairpin structure whose induced flow field 'ejects' fluid away from the wall, it is possible that SV1 and SV2 are or were part of a large uplifted hairpin structure. In addition to the uplifted counter-rotating vortical structures, also transverse vortices (such as denoted by 'TV' in figures 6 and 7) spanning the width of the VOI were observed. Note that TV is characterized by $\omega_3^+ < 0$ and rotates in the clockwise direction about the x_3-axis (as defined for a right-handed Cartesian coordinate system). Just upstream, it 'sweeps' fast-moving fluid towards the wall.

3.2. *Sphere dynamics*

A total of four spheres, denoted by S_1, S_2, S_3 and S_4, were tracked in separate data sets. Their diameters ranged from 7.3 mm to 8.3 mm, and normalized by inner wall scaling were $D^+ = 66$ (S_1), 73 (S_2), 72 (S_3) and 75 (S_4). Although only a finite number of spheres were tracked over the entire VOI, their total time trace represents approximately 1000 Kolmogorov time scales.

3.2.1. *Sphere translation*

The centroid positions of each sphere were tracked in space and time as described in § 2.2, and the normalized wall-normal and transverse sphere centroid positions, $x_{2,c}^+$ and $x_{3,c}^+$, as
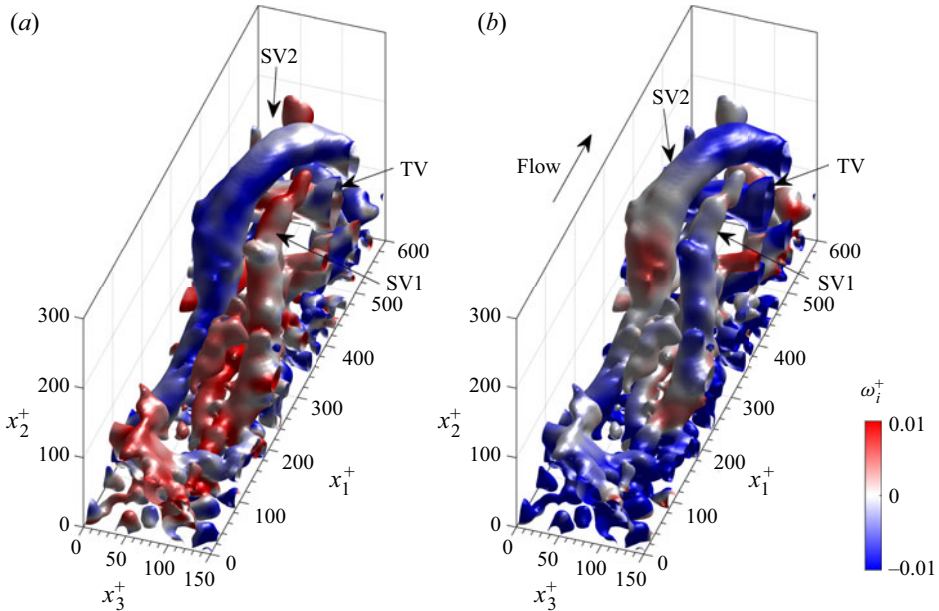
Figure 6. Example snapshot of Q-criterion iso-surfaces visualizing the coherent structures detected in the undisturbed TBL. Iso-surfaces are overlaid by (*a*) the normalized transverse vorticity ω_1^+, and (*b*) the normalized streamwise vorticity ω_3^+. An animation (supplementary movie 1) depicting the snapshot at different angles is available at https://doi.org/10.1017/jfm.2022.477.
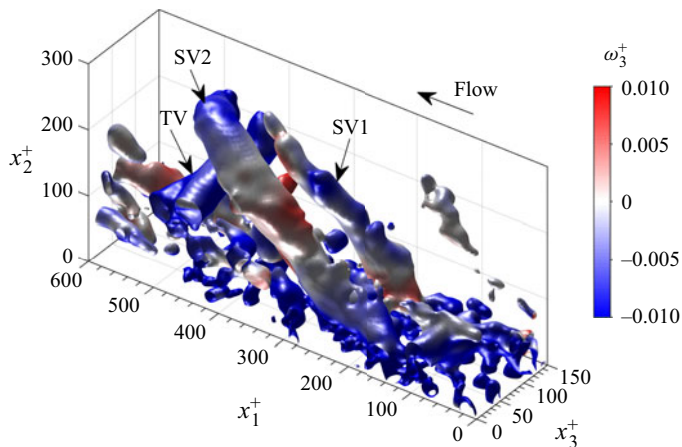

Figure 7. Same snapshot as depicted in figure 6(*b*) but at a different viewing angle.

a function of the sphere's streamwise centroid position $x_{1,c}^+$, are depicted in figure 8. Both the raw and the smoothed data are depicted, showing that smoothing (see § 2.2.2) removes random noise without altering trends. The vertical 'error' bar associated with sphere S_4 in figure 8(*a*) indicates its actual size ($D^+ = 75$). The transverse extent of the VOI was in the range $0 \leq x_3^+ \leq 150$ (the border at $x_3^+ = 0$ is indicated by a horizontal dashed line in figure 8*b*), and while in most cases the sphere centroid positions were located within the confines of the VOI, S_1 and S_2 were partially outside of it.
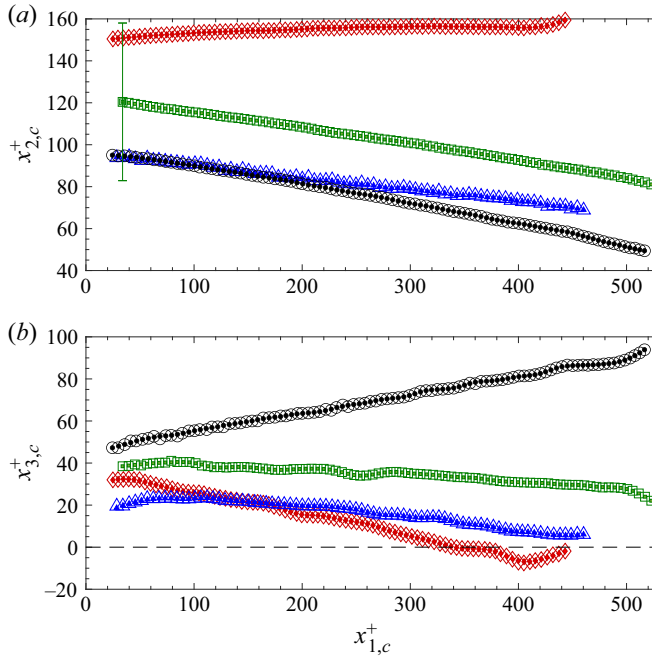
944 A12-12

Figure 8. Sphere wall-normal and transverse centroid positions in inner wall units as functions of $x_{1,c}^+$: (*a*) $x_{2,c}^+$, and (*b*) $x_{3,c}^+$. Red diamonds, S_1; blue triangles, S_2; black circles, S_3; green squares, S_4. Open symbols, raw data; filled symbols, smoothed data. Uncertainty is smaller than the marker size. The vertical error bar in (*a*) at the start of the trajectory of S_4 indicates the sphere diameter. The black dashed horizontal line in (*b*) indicates the edge of the VOI.

Spheres S_2, S_3 and S_4 were located closest to the wall (figure 8*a*) and moved towards it (all spheres entered the VOI below $x_2^+ = 130$). In contrast, sphere S_1 (red markers in figure 8*a*) entered the VOI at $x_2^+ \approx 150$ and remained at almost the same height. We will see in the following sections that the different sphere motion is the result of differences in the flow field in the spheres' vicinity and consequently different forcing on the spheres. Note that due to their relatively large size, the spheres are mostly immersed in the logarithmic layer, and none of them comes into contact with the wall. Even S_3 (black markers in figure 8*a*), which comes closest to the wall ($x_{2,c}^+ = 50$ at $x_{1,c}^+ = 520$; see figure 8*a*) and almost penetrates the viscous sublayer, is still partially inside the logarithmic layer. As a result, the finite-sized spheres are exposed to different turbulence characteristics in the buffer and the logarithmic layers, and varying velocity gradients act on them. In the transverse direction (figure 8*b*), S_2 and S_4 hardly change position (less than 10 wall units) upon traversing the VOI, while S_1 and S_3 exhibit considerable transverse displacements of approximately 40 and 50 wall units ($\sim D^+$), respectively. The latter displacements are approximately 10 % of the corresponding streamwise distance travelled, in agreement with the measurements by Tee *et al.* (2020). Note that spanwise migration implies spanwise forcing on the sphere, as will be discussed further in § 3.4.

The normalized instantaneous streamwise, wall-normal and transverse sphere centroid velocities are plotted in figures 9 and 10 as functions of $x_{1,c}^+$ for all tracked spheres. Both sphere velocities based on the smoothed centroid positions as well as those based on the derivatives of locally least-squares fitted second-order polynomials are depicted.
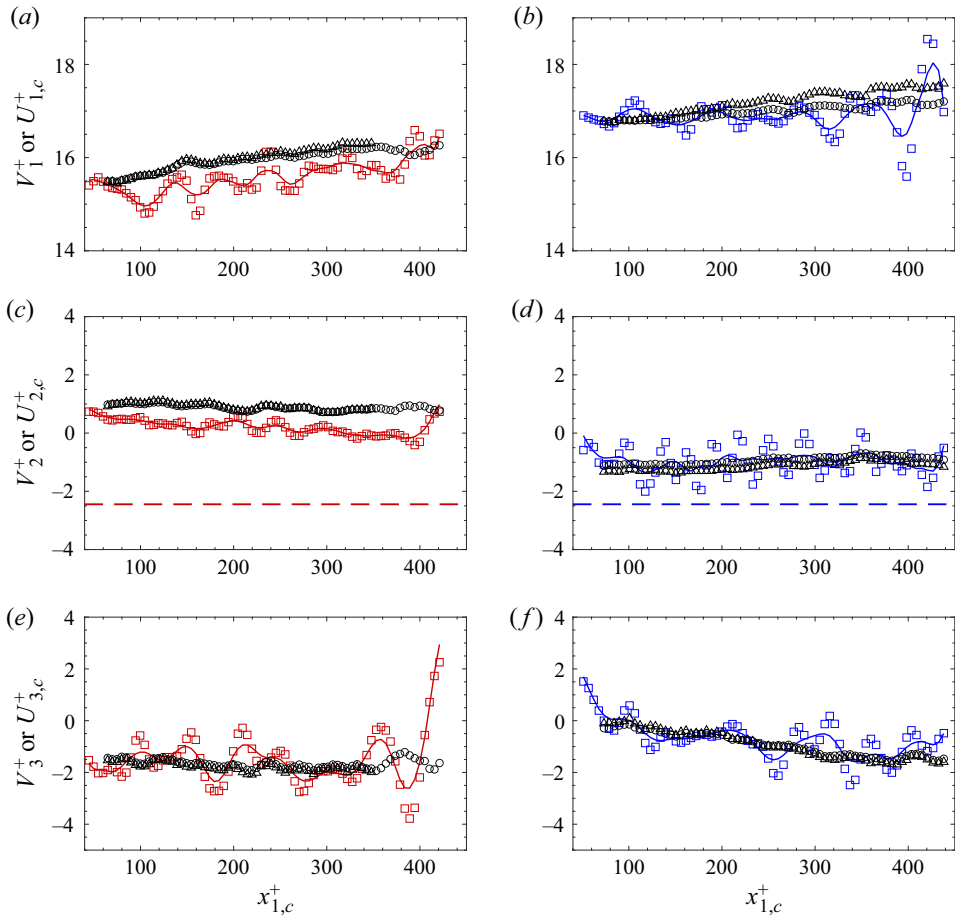
944 A12-13

Figure 9. Normalized instantaneous sphere centroid velocity components of S_1 (a,c,e) and S_2 (b,d,f), and the 'undisturbed' fluid velocities at the spheres' centroid positions as functions of $x_{1,c}^+$ in the streamwise (a,b), wall-normal (c,d), and transverse (e,f) directions. V_i^+ is based on: squares, smoothed sphere centroid positions; solid curves, derivatives of the least-squares fitted second-order polynomial; triangles, $U_{i,c}^{c+}$; circles, $U_{i,c}^{v+}$. The dashed horizontal line in (c,d) denotes the sphere's settling velocity in a quiescent fluid. Uncertainties of V_i^+ estimated by the r.m.s. values of the difference between the sphere centroid velocities based on the raw data and the smoothed (local polynomial fit) data, $\pm(\delta V_1^+, \delta V_2^+, \delta V_3^+)$, are (0.39, 0.25, 0.60) for S_1, and (0.40, 0.99, 0.49) for S_2.

For comparison, the calculated quiescent settling velocity, $V_s = (\rho_s - \rho)D^2 g/(18\mu)$, is also plotted as a horizontal dashed line in figures 9(c,d) and 10(c,d). As expected, the curves of sphere velocities determined based on the derivatives of locally fitted second-order polynomials (solid lines in figures 9 and 10) are smoother than those based on a central difference scheme. However, the trends are conserved. The uncertainties of V_i^+ estimated by the r.m.s. values of the difference between $V_{i,c}^+$ based on the raw data and based on the local polynomial fit are presented in the captions of figures 9 and 10.

The instantaneous components of the 'undisturbed' water velocity vectors U_c, based on the two methods discussed in § 2.2, are also plotted in figures 9 and 10. It can be observed that although the two methods lead to slightly different results, overall they
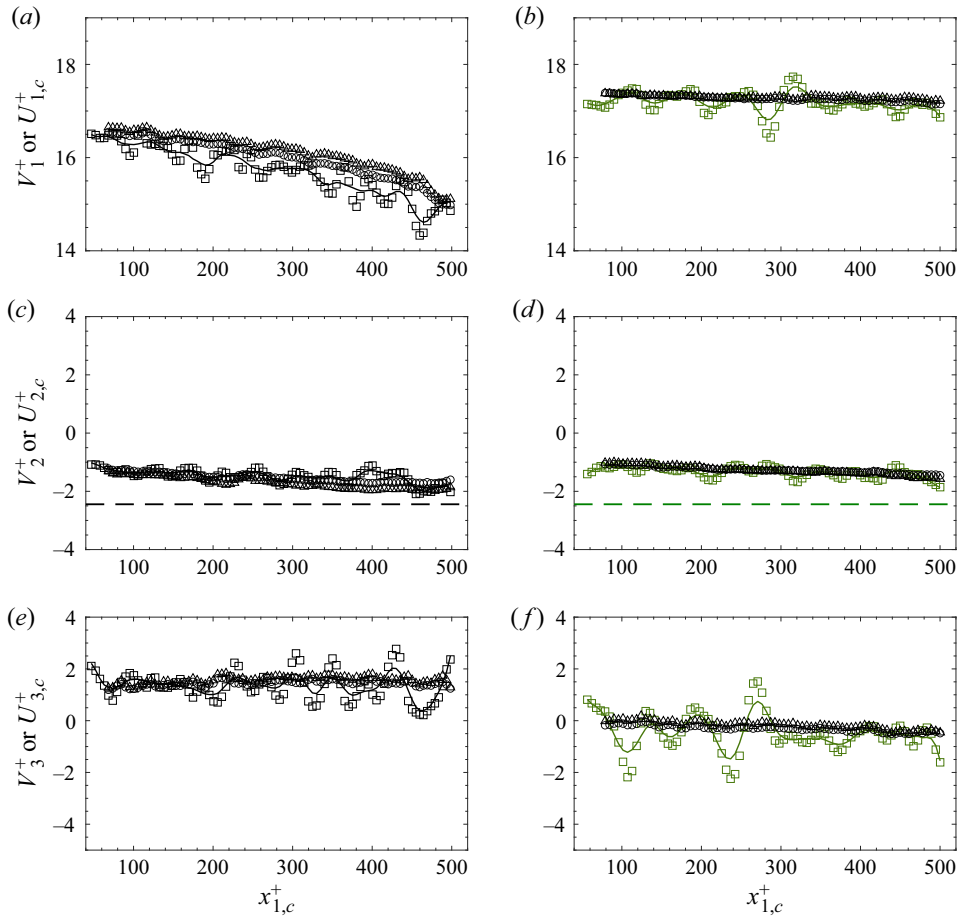
Figure 10. Normalized instantaneous sphere centroid velocity components of S_3 (a,c,e) and S_4 (b,d,f), and the 'undisturbed' fluid velocities at the spheres' centroid positions as functions of $x_{1,c}^+$ in the streamwise (a,b), wall-normal (c,d), and transverse (e,f) directions. V_i^+ is based on: squares, smoothed sphere centroid positions; solid curves, derivatives of the least-squares fitted second-order polynomial; triangles, $U_{i,c}^{c+}$; circles, $U_{i,c}^{v+}$. The dashed horizontal line in (c,d) denotes the sphere's settling velocity in a quiescent fluid. Uncertainties of V_i^+ estimated by the r.m.s. values of the difference between the sphere centroid velocities based on the raw data and the smoothed (local polynomial fit) data, $\pm(\delta V_1^+, \delta V_2^+, \delta V_3^+)$, are (0.48, 0.19, 0.72) for S_3, and (0.26, 0.15, 0.42) for S_4.

compare well. Only for sphere S_3 ($U_{1,c}^+$ in figure 10a) and S_2 ($U_{1,c}^+$ and $U_{2,c}^+$ in figures 9b,d) are small differences observed, and volume-averaged values of $U_{1,c}^+$ are lower than those interpolated onto the sphere centroid position, and vice versa for $U_{2,c}^+$. This is likely because S_2 and S_3 were closest to the wall (figure 8a), where the velocity gradients were strongest. Note that in all other cases, values of $U_{i,c}^+$ based on both methods nearly collapse.

Looking at the changes in V_1^+ (figures 9a,b and 10a,b), it is observed that only for S_3 (figure 10a) does V_1^+ decrease upon approaching the wall from about $V_1^+ \approx 16.5$ at $x_{1,c}^+ = 50$ ($x_{2,c}^+ \approx 94$) to $V_1^+ \approx 15$ at $x_{1,c}^+ \approx 500$ ($x_{2,c}^+ \approx 51$). The corresponding values of the undisturbed average streamwise water velocity (figure 4) are similar and are given by

944 A12-15

	$(U_{1,r}^+)'$	$\bar{U}_{1,r}^+$	$(U_{2,r}^+)'$	$\bar{U}_{2,r}^+$	$(U_{3,r}^+)'$	$\bar{U}_{3,r}^+$
S_1	0.43	-0.38	0.72	-0.69	0.93	0.18
S_2	0.29	-0.07	0.20	-0.04	0.37	0.12
S_3	0.32	-0.29	0.16	0.04	0.38	-0.10
S_4	0.16	-0.09	0.14	-0.08	0.50	-0.22

Table 1. Summary of the values of $(U_{i,r}^+)'$ and $\bar{U}_{1,r}^+$ for all investigated spheres.

$\langle \bar{U}_1 \rangle^+ = 14.6$ and 16.1 at $x_2^+ = 51$ and 93, respectively. In contrast, S_2 and S_4, which also move towards the wall (figure 8a), have nearly constant V_1^+ – i.e. $V_1^+ \approx 17.2$ and 17.0 for S_2 and S_4, respectively – and they move faster than the mean water flow at the same height (figure 4) for most of their trajectory. Only S_1, which moves slightly away from the wall (figure 8(a), $x_{2,c}^+ \approx 150$), increases its streamwise velocity from $V_1^+ \approx 15$ to $V_1^+ \approx 16$ (figure 9a), moving slower than the mean water velocity at this height ($\langle \bar{U}_1 \rangle^+ = 17.2$ at $x_{2,c}^+ = 150$; figure 4). Note that S_1, which enters the VOI farthest from the wall, has a streamwise velocity that is lower than those of S_2, S_3 and S_4 (figures 9a,b and 10a,b). Based on the mean streamwise water velocity profile (see figure 4) and the sphere's wall-normal position, one would expect it to be advected at a higher velocity. However, since $-\langle \overline{u_1 u_2} \rangle^+ > 0$ (see figure 5c), a negative correlation between u_1 and u_2 dominates, and S_1 is advected by relatively slow-moving fluid as indicated by the accompanying values of $U_{1,c}^+$.

Streamwise velocity components of S_1 and S_3 (figures 9a and 10a) clearly lag the interpolated 'undisturbed' water velocities along the trajectories, resulting in a drag force acting on the sphere in the streamwise direction, as will be discussed in § 3.4. Note that only in the case of S_1 (figure 9b) does V_2^+ lag $U_{2,c}^+$ along its trajectory, resulting in an upward-directed drag force (see § 3.4) inhibiting wall-ward motion (figure 8a). In all other cases, values of V_i^+ fluctuate around those of $U_{i,c}^+$. An indication of the differences between the sphere and fluid velocities at the sphere's position is provided by the r.m.s. values of $U_{i,r}^+$ ($= V_i^+ - U_{i,c}^{v+}$, with V_i^+ based on the smoothed data) and the averages along the sphere trajectories, $\bar{U}_{i,r}^+$, as summarized in table 1 for the different spheres. Values of $\bar{U}_{1,r}^+$ show that on average, in all cases the spheres lag the fluid, while in the transverse and wall-normal directions, this is not necessarily the case. Further note that similar magnitudes of $(U_{1,r}^+)'$ and $\bar{U}_{1,r}^+$ indicate that the spheres either lag ($\bar{U}_{1,r}^+ < 0$) or exceed ($\bar{U}_{1,r}^+ > 0$) the fluid for most of their trajectories.

The instantaneous wall-normal velocities of the spheres (figures 9c,d and 10c,d) are in accordance with the direction of their wall-normal motion (see figure 8a), i.e. for S_1, $V_2^+ > 0$, and in all other cases, $V_2^+ < 0$. Another interesting point to notice is that for the spheres that move towards the wall (S_2, S_3 and S_4), $|V_2^+| \approx 0.5|U_s|$, indicating that besides the net buoyancy force, additional forces opposing gravity, such as drag and lift forces, must be important, as will be discussed further in § 3.4. Note that this result is different from measurements reported by Tee *et al.* (2020), who found that wax spheres ($D^+ = 58 \pm 2$, $\rho_s/\rho = 1.006 \pm 0.003$) with characteristics similar to those of the present hydrogels, suspended in a TBL ($Re_\tau = 680$), descended at almost $2|U_s|$. Physically, this

944 A12-16

	f_1 (Hz)	Sr_1	f_2 (Hz)	Sr_2	f_3 (Hz)	Sr_3
S_1	27.8	52	36.4	41	24.0	21
S_2	22.0	68	38.9	174	31.8	77
S_3	27.8	77	29.9	165	30.0	70
S_4	22.7	130	26.1	171	27.3	50

Table 2. Summary of the estimated frequencies f_i and Strouhal numbers $Sr_i = f_i D/(U_{i,r}^v)'$ associated with the fluctuating sphere velocities.

means that the spheres must be exposed to a significant downward fluid impulse that was not observed for the spheres investigated here.

The magnitudes of V_3^+ (figures 9*e*,*f* and 10*e*,*f*) are of the same order of magnitude as those of V_2^+ (figures 9*c*,*d* and 10*c*,*d*). In accordance with their spanwise displacement (figure 8*b*), spheres S_1 and S_3 exhibited higher values of $|V_3^+|$ (figures 9*e* and 10*e*) than spheres S_2 and S_4, for which $V_3^+ \approx 0$ (figures 9*f* and 10*f*). Our results indicate that spanwise motion may be significant and should not be neglected, in agreement with Tee *et al.* (2020).

In all cases, it can be observed in figures 9 and 10 that the sphere velocities exhibit fluctuations along their tracks with amplitudes exceeding the estimated uncertainties (see captions of figures 9 and 10). The estimated frequencies f_i ($i = 1, 2, 3$), and Strouhal numbers based on the r.m.s. values of the components of the relative velocities, $Sr_i = f_i D/(U_{i,r}^v)'$ ($i = 1, 2, 3$), are summarized in table 2. Note that Tee *et al.* (2020) also reported sphere velocities that fluctuated, which they attributed to vortex shedding ($Re_s > 100$). In the present case, Strouhal numbers are much higher than those associated with vortex shedding in the wake of a sphere in a uniform flow ($0.1 < Sr < 0.2$). Note that Tee *et al.* (2020) did not measure the instantaneous flow field in the vicinity of the spheres, and their Strouhal numbers were based on the mean, 'undisturbed' streamwise water velocity at the sphere's centroid position. This will overestimate Re_s and result in lower Sr than when the actual slip velocity is accounted for. In the present measurements, the instantaneous sphere Reynolds numbers $Re_s = |U_r|D/\nu$, based on the magnitude of the instantaneous relative velocity vector, is mostly in the range $10 \leq Re_s \leq 80$ (see figure 11), while $\overline{Re_s} = 63$, 36, 31 and 35 for S_1, S_2, S_3 and S_4, respectively. Since for spheres exposed to a uniform flow, flow separation occurs at $Re_s \approx 25$ (Taneda 1956), small wake oscillations start at $Re_s \approx 130$, and unsteady vortex shedding starts at $Re_s \approx 270$ (Sakamoto & Haniu 1990), it is unlikely that vortex shedding played a role here. However, flow separation may occur, and in conjunction with the unsteady TBL flow might lead to oscillations in sphere velocities. Furthermore, as a result of the surrounding turbulence, the onset of flow separation and vortex shedding may occur at a lower Re_s value. However, we did not observe any signs of this in the measured 3-D flow field as discussed further in § 3.4.

Another mechanism that may lead to fluctuations in sphere velocities is the forcing provided by the turbulence in the vicinity of the spheres. The turbulence time scales can be estimated based on (i) the viscous time scale $\tau_v = \nu/u_\tau^2$, and (ii) the Kolmogorov time scale $\tau_k = (\nu/\epsilon)^{1/2}$, where ϵ is the turbulent kinetic dissipation rate that can be estimated in the log layer by $\epsilon \approx \overline{u_1 u_1}(\partial \bar{U}_1/\partial x_2)/3$ (Pope 2000). Based on the present data (summarized in table 3), this leads to $f_v(= 1/\tau_v) = 81$ Hz, and $f_k(= 1/\tau_k) = 22$ and 12.7 Hz at $x_2^+ = 50$ and 100, respectively. Although these are crude estimates, the
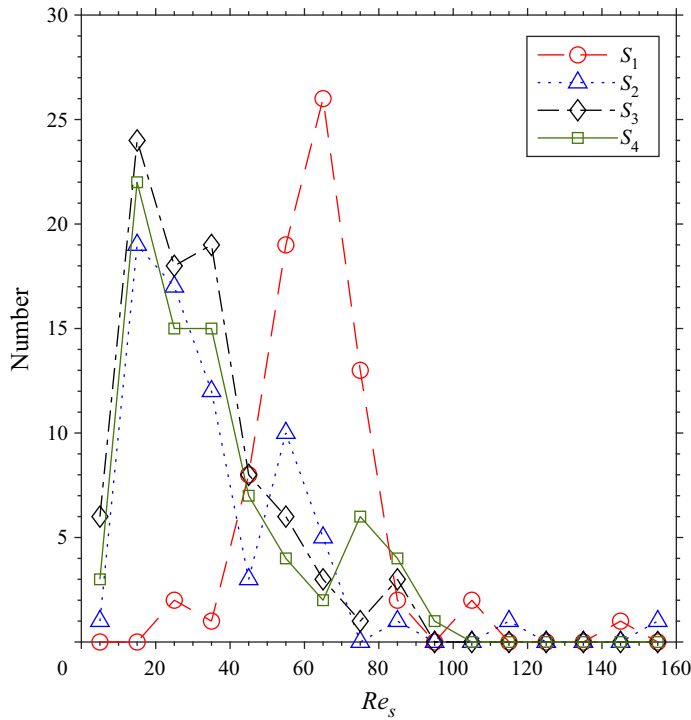
944 A12-17

Figure 11. Histograms of the instantaneous sphere Reynolds numbers, Re_s, for all four spheres. Data points are located at the centres of the bins (bin size 10).

x_2^+	$\partial\langle \bar{U}_1\rangle/\partial x_2$ (s^{-1})	$\langle\overline{u_1 u_1}\rangle \times 10^6$ $(\mathrm{m}^2\,\mathrm{s}^{-2})$	$\epsilon \times 10^6$ $(\mathrm{m}^2\,\mathrm{s}^{-3})$	η_k $(\mu\mathrm{m})$	$f_k = 1/\tau_k$ (Hz)
50	3.95	364.5	480	213.6	22
100	2.0	243.0	162	280	12.7

Table 3. Summary of the estimated scales in the log layer.

f_i (table 2) are of the same order of magnitude as f_v and f_k, supporting our hypothesis. Note further that we validated that these frequencies were not an artefact of the applied local regression detailed in § 2.2.

3.2.2. *Sphere rotation*

The angular velocities of the sphere, $\dot{\alpha}_i$, were determined by the ICP algorithm as described in § 2.2. Based on the interpolated water velocity vector field (see § 2), the streamwise, wall-normal and transverse components of $\boldsymbol{\omega}_c$ were calculated and similar as for $\boldsymbol{U}_c$, $\boldsymbol{\omega}_c$ was evaluated as the volume-averaged value at the sphere's centroid. The components of the water angular velocities based on $\boldsymbol{\omega}_c$ and normalized in inner wall scaling are given by $\Omega_{i,c}^+ = (\omega_{i,c}\nu)/(2u_\tau^2)$, while the normalized angular sphere velocities are given by $\dot{\alpha}_i^+ = (\dot{\alpha}_i\nu)/u_\tau^2$ ($i = 1, 2, 3$).
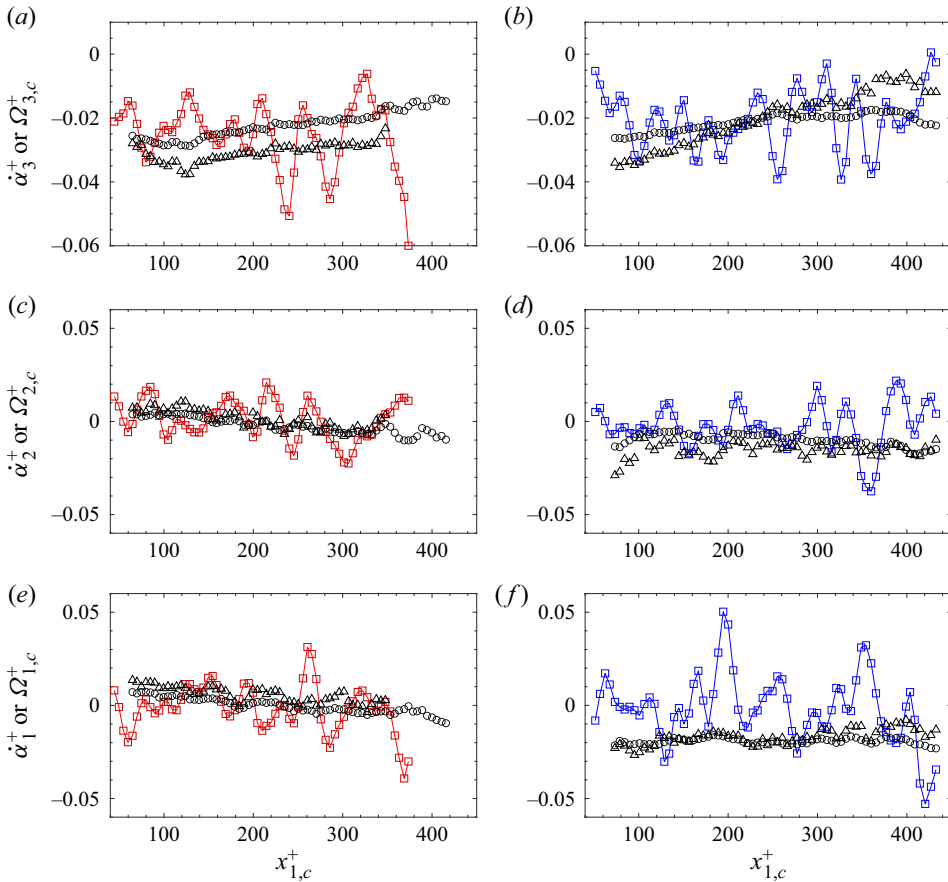
944 A12-18

Figure 12. Instantaneous normalized angular velocities of the sphere and the water versus $x_{1,c}^+$ for S_1 (*a,c,e*) and S_2 (*b,d,f*). Squares indicate sphere angular velocities $\dot{\alpha}_i^+$ based on smoothed data. Water angular velocities at the sphere position are given for: $\Omega_{i,c}^{v+}$, circles; and $\Omega_{i,c}^{c+}$, triangles. Rotation is about: (*a,b*) x_3, (*c,d*) x_2, (*e,f*) x_1.

The results for $\dot{\alpha}_i^+$ (smoothed), $\Omega_{i,c}^{v+}$ and $\Omega_{i,c}^{c+}$ are plotted in figures 12 and 13 as functions of $x_{i,c}^+$ for spheres S_1, S_2 and S_3, S_4, respectively. Average values of $\dot{\alpha}_i^+$ and $\Omega_{i,c}^{v+}$ are summarized in table 4. All four spheres exhibited negative (clockwise) angular velocities about the x_3-axis ($\dot{\alpha}_3^+ < 0$, figures 12*a,b* and 13*a,b*, and $\overline{\dot{\alpha}_3^+} < 0$ in table 4) in accordance with the positive mean shear rate near the wall. Water angular velocity components mostly have the same signs as those of the spheres, and in most cases the rotational motion of the spheres lags that of the fluid (see table 4). Values of $\Omega_{i,c}^{v+}$ clearly differ in magnitude from $\Omega_{i,c}^{c+}$, especially for rotation about x_3 (figures 12*a,b* and 13*a,b*), and in most cases, $\Omega_{i,c}^{v+} < \Omega_{i,c}^{c+}$. This is the result of significant spatial non-uniformity of the vorticity at the sphere's position as it is immersed in the buffer and log layer of the TBL, where turbulence is most active. In the case of high spatial non-uniformity, and taking the finite size of the spheres into account, one may argue that the volumetric mean presents a better estimate than the value evaluated at the sphere centroid. Sphere S_3, which is located closest to the wall, has the highest magnitude of $\overline{\dot{\alpha}_3^+}$, followed by S_1, while S_2
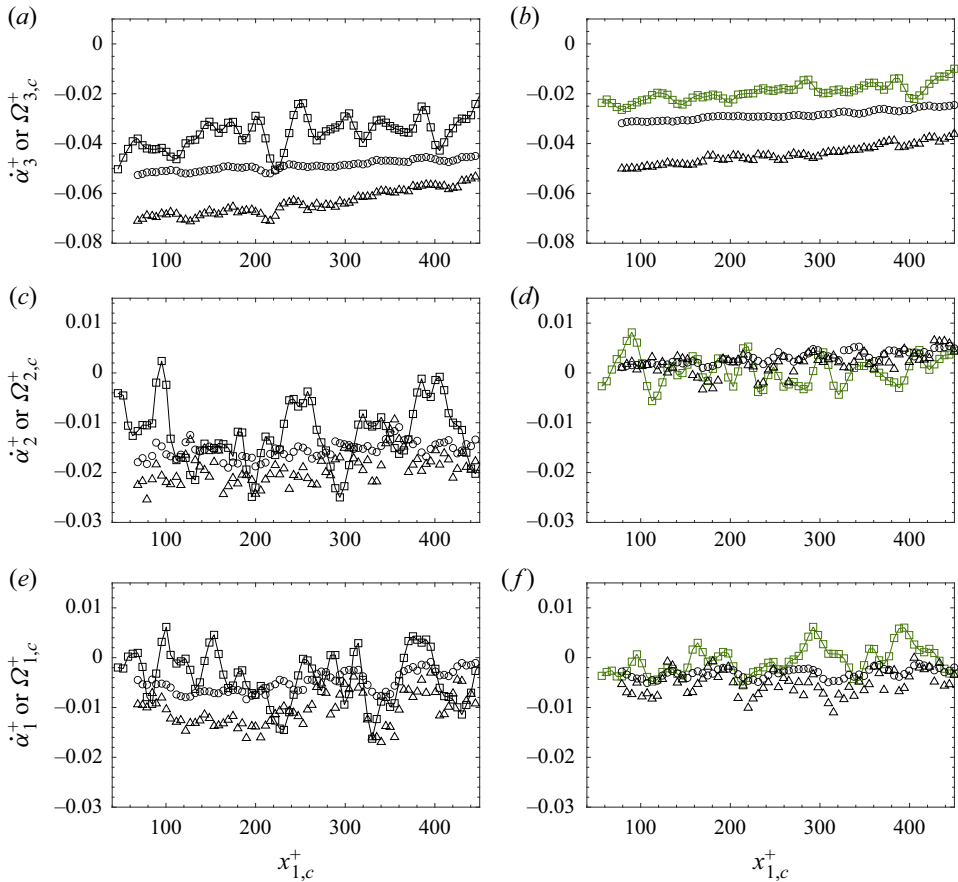
944 A12-19

Figure 13. Instantaneous normalized angular velocities of the sphere and the water versus $x_{1,c}^+$ for S_3 (a,c,e) and S_4 (b,d,f). Squares indicate sphere angular velocities $\dot{\alpha}_i^+$, based on smoothed data. Water angular velocities at the sphere position are given for: $\Omega_{i,c}^{v+}$, circles; and $\Omega_{i,c}^{c+}$, triangles. Rotation is about: (a,b) x_3, (c,d) x_2, (e,f) x_1.

	$\overline{\dot{\alpha}_3^+}$ $(\times 10^{-3})$	$\overline{\dot{\alpha}_2^+}$ $(\times 10^{-3})$	$\overline{\dot{\alpha}_1^+}$ $(\times 10^{-3})$	$\overline{\Omega_{3,c}^{v+}}$ $(\times 10^{-3})$	$\overline{\Omega_{2,c}^{v+}}$ $(\times 10^{-3})$	$\overline{\Omega_{1,c}^{v+}}$ $(\times 10^{-3})$
S_1	-28.9	3.0	-2.7	-22.1	-2.3	-0.26
S_2	-20.63	-2.6	-1.7	-21.3	-9.8	-19.3
S_3	-35.3	-12.1	-4.5	-48.3	-15.4	-4.4
S_4	-18.8	0.63	-0.41	-28.1	3.1	-2.9

Table 4. Summary of angular sphere and water velocities averaged over the spheres' trajectories.

and S_4 rotate the slowest about x_3 (see table 4). Note that the importance of the combined shear-, wall- and rotation-induced lift forces on the wall-normal motion of the spheres is discussed further in § 3.4.

In all cases, sphere angular velocities about the x_1- and x_2-axes ($\dot{\alpha}_1^+$ and $\dot{\alpha}_2^+$ in figures 12 and 13) are small, and mean values are substantially smaller than those about the x_3-axis

	$\overline{\Omega_{3,r}^{v+}}$ ($\times 10^{-3}$)	$\overline{\Omega_{2,r}^{v+}}$ ($\times 10^{-3}$)	$\overline{\Omega_{1,r}^{v+}}$ ($\times 10^{-3}$)
S_1	-7.4 ± 17.7	5.1 ± 16.7	-2.2 ± 13.1
S_2	0.16 ± 9.7	7.0 ± 12.5	17.1 ± 18.0
S_3	13.4 ± 5.1	3.1 ± 6.2	-0.3 ± 5.8
S_4	9.5 ± 2.3	-2.5 ± 3.3	2.7 ± 3.1

Table 5. Summary of the average values of the relative angular velocities. Standard deviations are depicted as uncertainties.

(see table 4). Only for S_3 is $\overline{\dot{\alpha}_2^+}$ significant ($\approx 0.3\overline{\dot{\alpha}_3^+}$; see table 4) and the importance of the rotation-induced lift force acting in the transverse direction (see figure 8b) will be discussed in § 3.4. The mean values of the relative angular velocities along the different sphere tracks, $\overline{\Omega_{i,r}^{v+}} = \dot{\alpha}_i^+ - \Omega_{i,c}^{v+}$ ($i = 1, 2, 3$) including their standard deviations, are summarized in table 5. Values illustrate that the $\overline{\Omega_{i,r}^{v+}}$ vary significantly for the different spheres and display large standard deviations as a result of the different flow field characteristics in their immediate vicinity that are discussed next.

3.3. *Flow field in the vicinity of the spheres*

The present measurements allow us to determine simultaneously the instantaneous flow field in the vicinity of the spheres as well as their motion (see §§ 3.2.2 and 3.2.1). Since spheres S_3 and S_4 were fully resolved within the VOI (see figure 8), we will focus on them in this subsection.

3.3.1. *Sphere S_3*

Two instantaneous snapshots ($\Delta t^+ = 16.7$) of sphere S_3, including the instantaneous vortices overlaid by ω_1^+, are presented in figure 14 (and animations are provided in supplementary movie 2). As observed, S_3 is surrounded by a plethora of vortical structures. A group of fragmented transverse and inclined vortices within the dashed ellipse in figure 14(a) can be observed just upstream of S_3 upon entering the VOI. The inclination angle of this group is approximately $40\,^{\circ}$ from the bottom wall, agreeing well with typical inclination angles of hairpin packets observed in TBLs (Adrian 2007). However, no complete connected hairpin structures were observed. As the sphere traverses the VOI (figure 14b), most transverse vortices associated with the packet leave the VOI, and mainly streamwise-oriented longitudinal vortices rotating about the x_1-axis are observed (figure 14b). In particular, close to the wall just below and downstream of S_3, two counter-rotating longitudinal vortices denoted by 'LV1' ($\omega_1^+ > 0$) and 'LV2' ($\omega_1^+ < 0$) can be discerned in figure 14. They are located close to the wall inside the buffer layer ($x_2^+ < 50$) and extend up to $x_1^+ \approx 300$ in figure 14(a).

A close up of the sphere and parts of LV1 and LV2 are depicted in figure 15 at different viewing angles, revealing some interesting characteristics. First, LV1 and LV2 are not connected. Instead, just upstream of S_3, a transverse 'bridging' vortex located between $x_1^+ = 50$ and 80 (denoted 'TV1' in figure 15) connects to LV1 and extends in the negative x_3^+-direction up to the edge of the VOI ($x_3^+ = 0$). This suggests that LV1 and TV1 are part of a hairpin-like structure (Adrian 2007). Note that also LV2 is connected to a transverse
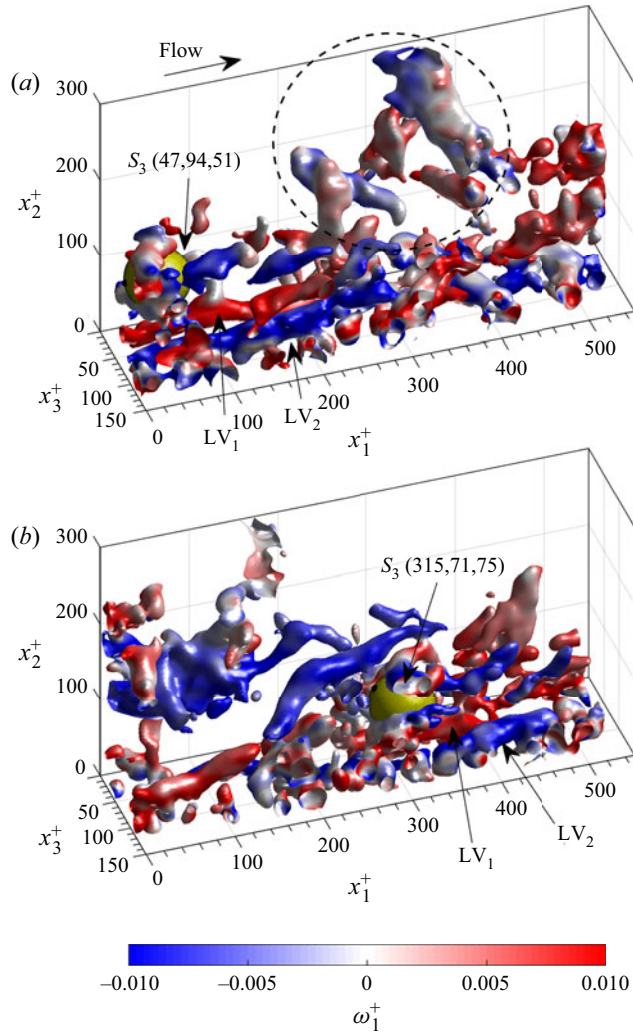
Figure 14. Two snapshots ($\Delta t^+ = 16.7$) of the instantaneous vortical structures in the vicinity of S_3 visualized by Q-criterion iso-surfaces overlaid by ω_1^+. The sphere's surface is depicted in yellow, with black markers to indicate its change in orientation. Values in parentheses denote ($x_{1,c}^+, x_{2,c}^+, x_{3,c}^+$). Supplementary movie 2 provides animations of the snapshot in (*a*) at different viewing angles.

vortical structure (denoted 'TV2' in figure 15) extending up to the edge of the VOI in the positive x_3^+ direction. The rotation directions of LV1, LV2, TV1 and TV2 that are indicated by the overlaid streamwise and transverse normalized vorticity components in figures 15(*a*) and 15(*b*), respectively, indicate that they generate downward-moving fluid just ahead of the sphere. This downward motion is responsible for the relatively strong wall-ward motion of S_3 (see figure 8(*a*) as well as figures 9 and 10).

This is investigated further by analysing snapshots ($\Delta t^+ = 5.5$) of equatorial wall-normal (x_1–x_3) and wall-parallel (x_1–x_2) planes moving with the sphere that depict the instantaneous correlations of water fluctuating velocities, $(u_1 u_2)^+$ (figures 16*a,c,e,g* and 17*a,c,e,g*). Here and in similar plots subsequently, the sphere's cross-section is indicated by a white circle, and its rotation in the depicted plane relative to
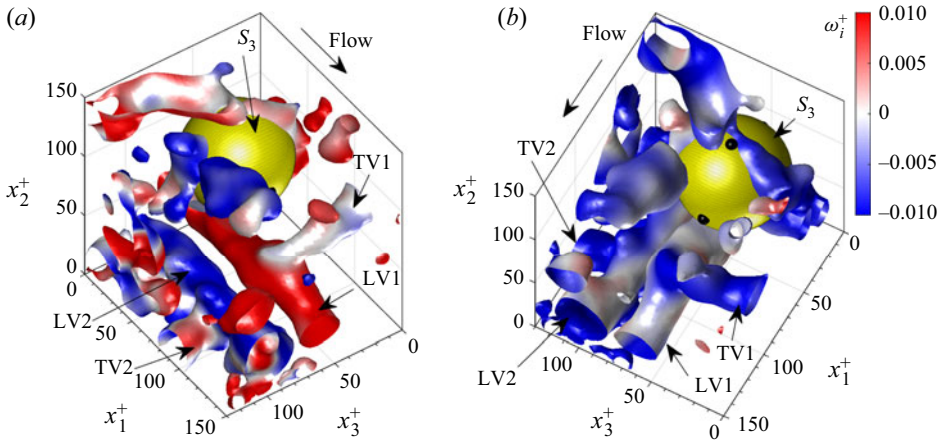
944 A12-22

Figure 15. Close-up of the snapshot of sphere S_3 in figure 14(*a*) at two different viewing angles. Vortical structures are visualized by Q-criterion iso-surfaces overlaid by (*a*) ω_1^+, and (*b*) ω_3^+. The sphere surface is depicted in yellow, with black markers indicating its orientation.

its initial orientation (denoted by a dashed line) is indicated by a rotated solid line extending from the sphere's centre. Contour plots of $(u_1u_2)^+$ (figures 16*a,c,e,g* and 17*a,c,e,g*) clearly show a large, highly coherent area where $(u_1u_2)^+ < 0$ just downstream of the sphere. Negative values of $(u_1u_2)^+$ may indicate both sweeps and ejections, and to determine to which quadrant they belong, contour plots of u_1^+ in the same equatorial planes are depicted in figures 16(*b,d,f,h*) and 17(*b,d,f,h*). Combining the plots of $(u_1u_2)^+$ and u_1^+, it becomes clear that just downstream of the sphere, the area associated with $(u_1u_2)^+ < 0$ correlates with $u_1^+ > 0$, indicating that sweeps induced by the combined action of the coherent structures (figures 14 and 15) dictate the flow field just downstream of S_3.

Besides the coherent sweep motion just downstream of S_3, it can be seen in the wall-parallel equatorial planes (figures 17*b,d,f,h*) that S_3 is exposed to transverse shear. This is especially clear in figures 17(*d,f*), where patches of positive and negative streamwise velocity fluctuations on opposite sides of S_3 are observed. The resulting shear-induced lift force will be discussed in § 3.4.

3.3.2. *Sphere* S_4

Similarly as for S_3, three snapshots ($\Delta t^+ = 13.7$) of the vortices in the vicinity of S_4 are depicted as Q-criterion iso-surfaces in figure 18, overlaid by ω_1^+ and by ω_3^+. Also in this case, several vortical structures characteristic of TBLs can be discerned. In particular, downstream of S_4, two counter-rotating, uplifted longitudinal vortices (denoted by 'LV3' and 'LV4' in figure 18) can be seen. LV4 is positioned above LV3 (see supplementary movies 3 and 4), and both are tilted with respect to the x_1^+-axis towards the x_3^+-axis. As S_4 traverses the VOI, downstream of it, a well-defined hairpin packet appears, consisting of four hairpin heads (denoted by 'HP1' to 'HP4' in figures 18*b,c*). Again due to the limited transverse extent of the VOI, only a part of the packet is resolved. All the hairpin heads rotate in the clockwise direction ($\omega_3^+ < 0$; figure 18*c*), in agreement with the direction of the mean shear. Note that the sphere is not overtaken by the hairpin packet as reported by van Hout (2013), who studied smaller ($D^+ \approx 10$) polystyrene beads, but instead remains
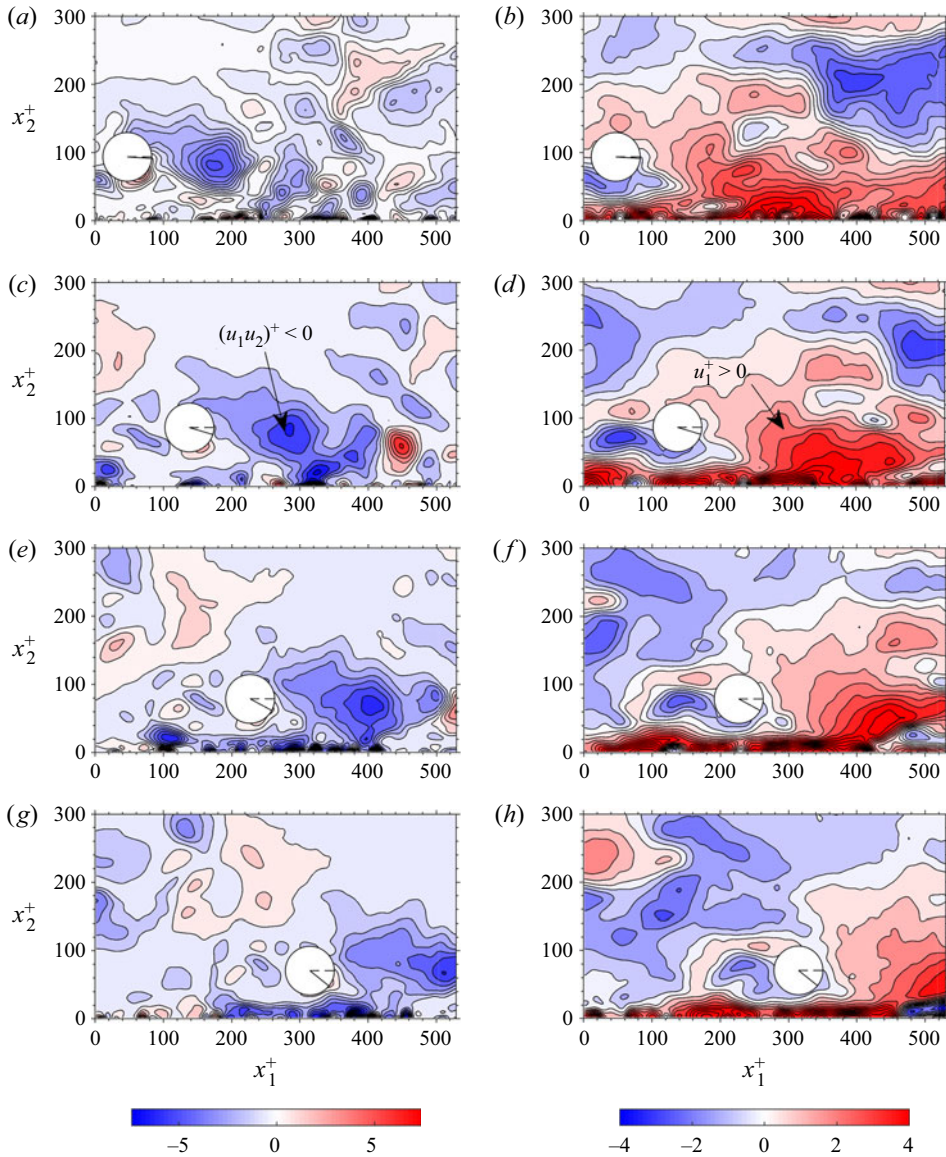
Figure 16. For S_3, a sequence ($\Delta t^+ = 5.5$) of equatorial wall-normal planes depicting the correlations of instantaneous water fluctuating velocities $(u_1 u_2)^+$ (a,c,e,g), and the streamwise water velocity fluctuating velocities u_1^+ (b,d,f,h). The hydrogel sphere is depicted as a filled white circle. Its initial orientation is indicated by a dashed line, while its changing orientation is indicated by a solid line.

positioned just upstream of the identified hairpin packet. However, it seems that the hairpin packet's development is hampered as S_4 moves towards the wall. Evidence for this can be found by looking at a close-up of the vortices in the vicinity of S_4 as shown in figure 19. This close-up shows that a somewhat distorted hairpin vortex is located below S_4 (denoted by 'HP5' in figure 19), and it is likely that HP5 is part of the identified hairpin packet upstream of S_4. However, the wall-ward motion of S_4 hinders the self-induced upward motion of HP5, and 'pushes' HP5 towards the wall. Note further that the 'legs' of HP5
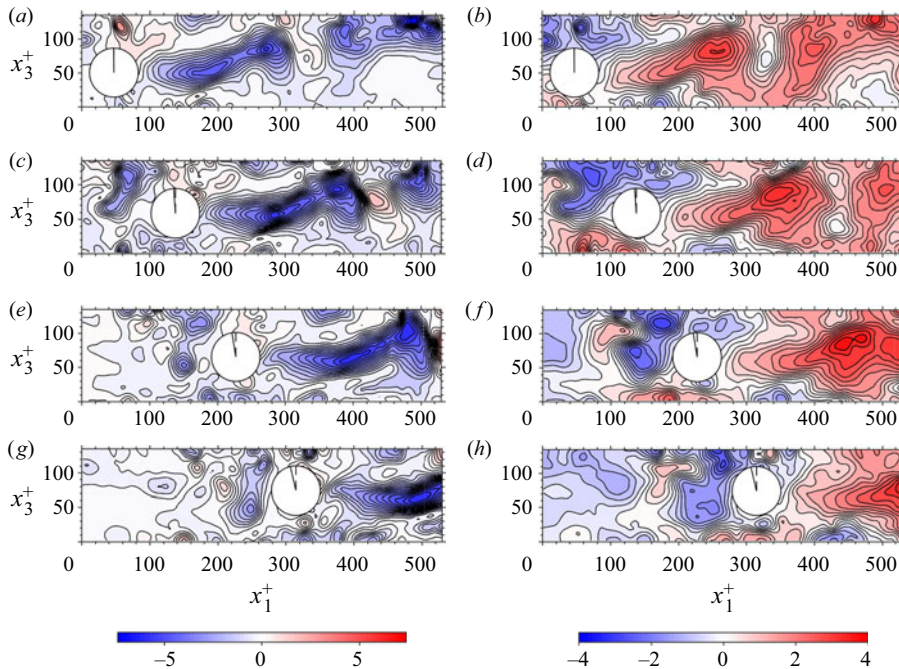
Figure 17. For S_3, a sequence ($\Delta t^+ = 5.5$) of equatorial wall-parallel planes depicting the correlations of the instantaneous water fluctuating velocities $(u_1 u_2)^+$ (*a,c,e,g*), and the streamwise water fluctuating velocities u_1^+ (*b,d,f,h*). The hydrogel sphere is superposed as a filled white circle. Its initial orientation is indicated by a dashed line, while its changing orientation is indicated by a solid line. Note that the view is from the wall upwards.

generate ejection motion that may explain why S_4 settles slightly slower than S_3 (see figure 10).

Wall-normal and wall-parallel equatorial planes depicting contour plots of $(u_1 u_2)^+$ and u_1^+ are presented in figures 20 and 21. Similarly as for S_3, also downstream of S_4 a distinct sweep (denoted by 'SW' in figure 20) is observed, most likely induced by LV4 (figure 18*b*). In addition, below SW and slightly downstream of it close to the wall, a clear ejection (denoted by 'EJ' in figure 20*a*) is seen. As S_4 traverses the VOI, it stays just upstream of the sweep (located just downstream of the slanted dashed line across figures 20*a,c,e,g*). Further note that the 'signature' of the hairpin packet (see figure 18*c*) becomes visible as a train of uplifted opposite sign patches of u_1^+ (dashed ellipse in figure 20*l*) induced by the hairpin heads HP1 to HP4 (figure 18*c*).

3.4. *Lift and drag forces acting on the spheres*

Sphere motion is dictated ultimately by the forces acting on it, amongst them the lift and drag forces that we focus on in this subsection. Inertial forces such as the fluid pressure, the Basset history force, and the added mass forces and their importance will be discussed at the end of this subsection. For the present range of Re_s (figure 11), the drag force acting on the spheres can be calculated by the quadratic drag relation given by (e.g. Yam *et al.* 2013)

$$\boldsymbol{F}_D = -C_D \, \frac{1}{2} \, \rho \, \frac{\pi D^2}{4} \, |\boldsymbol{U}_r| \, \boldsymbol{U}_r, \tag{3.1}$$
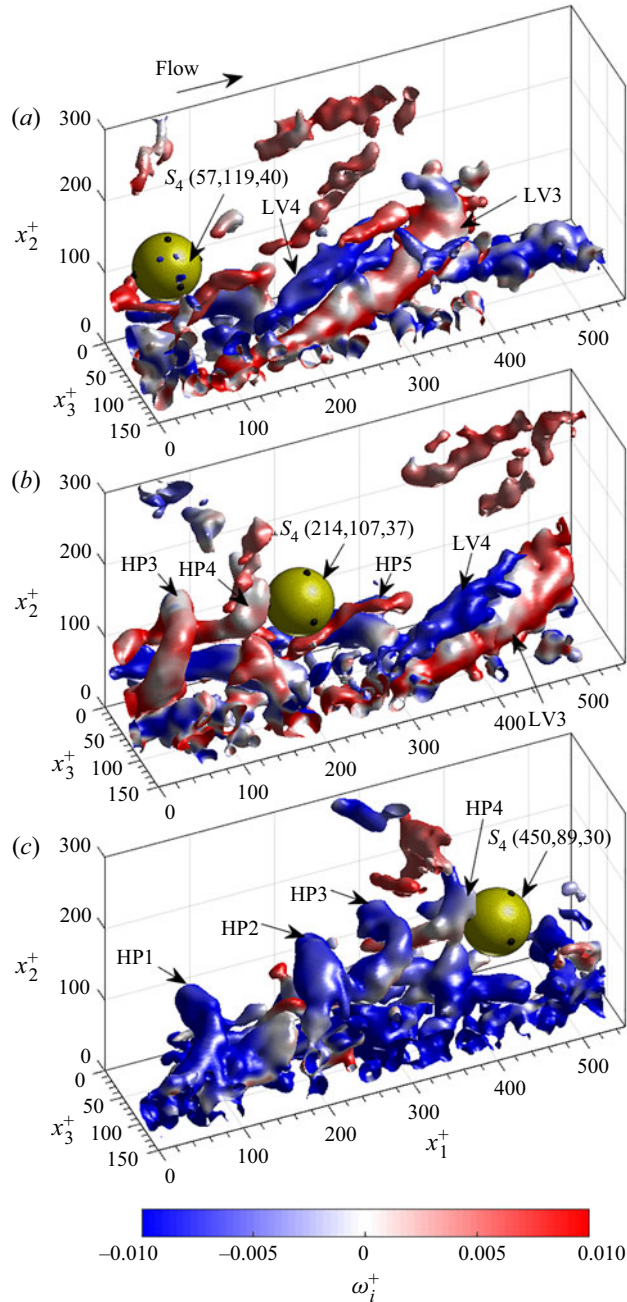
944 A12-25

Figure 18. Sequence of instantaneous vortical structures (visualized by Q-criterion iso-surfaces) in the vicinity of sphere S_4 ($\Delta t^+ = 16.7$). Iso-surfaces were overlaid by (a,b) ω_1^+, and (c) ω_3^+. The hydrogel sphere is depicted in yellow with black markers to indicate its change in orientation. The values in parentheses denote $(x_{1,c}^+, x_{2,c}^+, x_{3,c}^+)$. Supplementary movies 3 and 4 provide animations of the snapshots in (b,c) at different viewing angles.
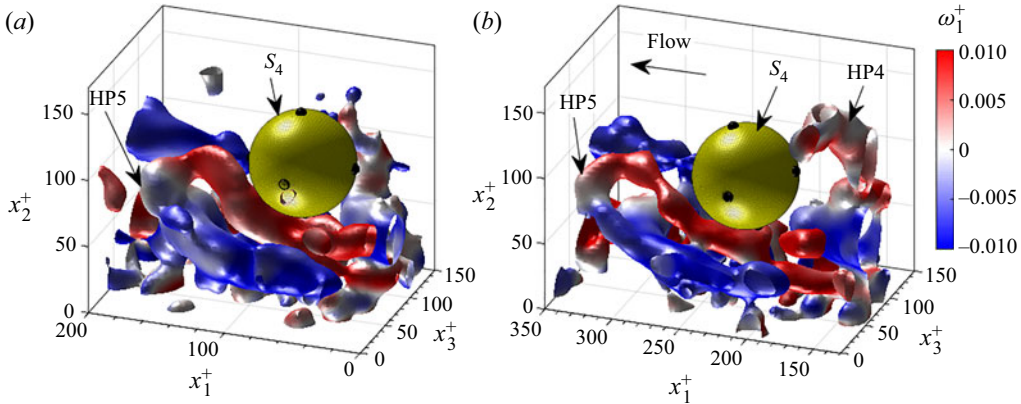
Figure 19. Close-up of vortical structures in the vicinity of S_4. Vortical structures were visualized by Q-criterion iso-surfaces that were overlaid by ω_1^+. Snapshots in (a,b) correspond to figures 18(a,b).

where C_D denotes the drag coefficient for spheres. In the present case, due to the effect of shear and wall proximity, as well as ambient turbulence (Zeng *et al.* 2009), C_D may be modified from the standard drag relation $C_{Do} = (24/Re_s)(1 + 0.15Re_s^{0.687})$ (Schiller–Naumann correlation, valid for $0.01 < Re_s < 1000$; Clift, Grace & Weber 1978). Zeng *et al.* (2009) and Shi *et al.* (2021) have proposed correlations for the drag and lift coefficients based on direct numerical simulations (DNS) studies of a stationary sphere in a wall-bounded linear shear flow and of a rigid sphere translating steadily near a wall, either in a fluid at rest or in the presence of a uniform shear, respectively. While the DNS by Shi *et al.* (2021) may be more relevant to the present study, their correlations are valid within a narrow range of the relative shear rate, $-0.5 \leq Sr\ (= (\partial U_1/\partial x_2)_c D/|U_r|) \leq 0.5$. In the case when $|U_r|$ becomes small, such as for nearly neutrally buoyant particles, magnitudes of Sr exceed this range easily. This is the case in the present study, where $|U_r|$ is small, and values of $|Sr|$ are an order of magnitude higher than the range for which the correlations proposed by Shi *et al.* (2021) are valid. Although maximum values in Zeng *et al.* (2009) are also bounded by $Sr = 2$, their correlations do not contain Sr explicitly. We therefore used the correlations proposed by Zeng *et al.* (2009) for the calculation of the lift and drag coefficients. Taking shear and wall proximity into account, Zeng *et al.* (2009) proposed the following correction to standard drag for a stationary sphere in a wall-bounded, linear shear flow:

$$C_D = C_{Do}(1 + \alpha\,Re_s^\beta), \tag{3.2}$$

where $\alpha = 0.15 - 0.046(1 - 0.16\delta^2)\exp(-0.7\delta)$, with the normalized sphere-to-wall gap given by $\delta = x_{2,c}/D - 0.5$, and $\beta = 0.687 + 0.066(1 - 0.76\delta^2)\exp(-\delta^{0.9})$. Note that when $\delta \to \infty$, $C_D = C_{Do}$.

Besides the drag, the lift force acting perpendicular to it may be of importance. However, in contrast to the drag, there is significant uncertainty regarding the validity of lift force correlations. In the Stokes limit, no lift forces act on the sphere even in the presence of a wall (Bretherton 1962). However, in the present measurements, Stokes flow cannot be assumed, and lift forces may play a role (see figure 11). For a rotating sphere in a shear flow close to a wall (Zeng *et al.* 2009), shear-induced, rotation-induced (so-called 'Magnus' force) and wall-induced lift forces may all be important. Starting with the early studies by Segre & Silberberg (1962) and Saffman (1965) for low Re_s and low shear rates, the
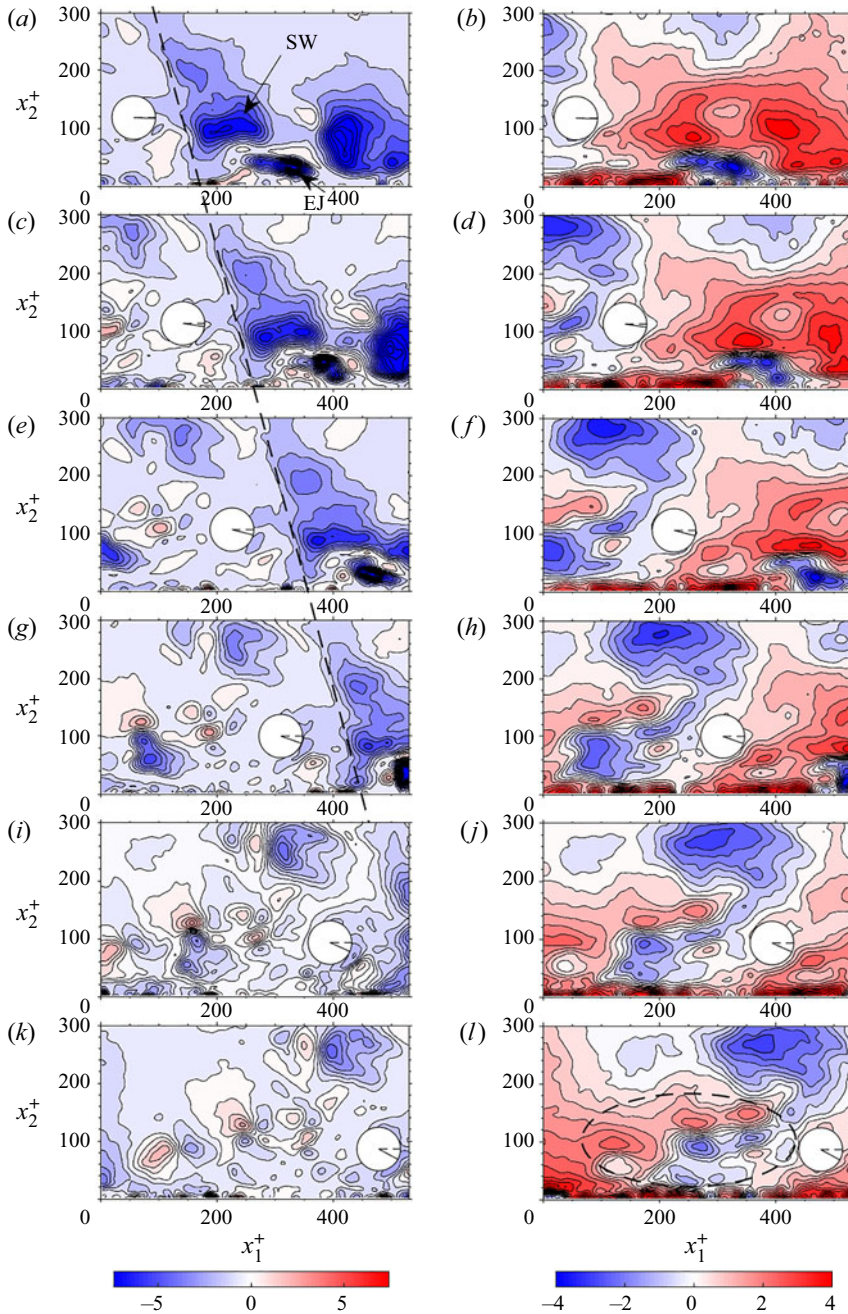
Figure 20. For S_4, a sequence ($\Delta t^+ = 4.9$) of equatorial wall-normal planes depicting the correlations of the instantaneous water fluctuating velocities $(u_1 u_2)^+$ (*a,c,e,g,i,k*), and the streamwise water fluctuating velocities u_1^+ (*b,d,f,h,j,l*). The hydrogel sphere is superposed as a filled white circle. Its initial orientation is indicated by a dashed line, while its changing orientation is indicated by a solid line. 'SW' and 'EJ' in (*a*) denote sweep and ejection motion, respectively. The slanted dashed line across (*a,c,e,g*) demarcates the upstream position of a sweep motion.
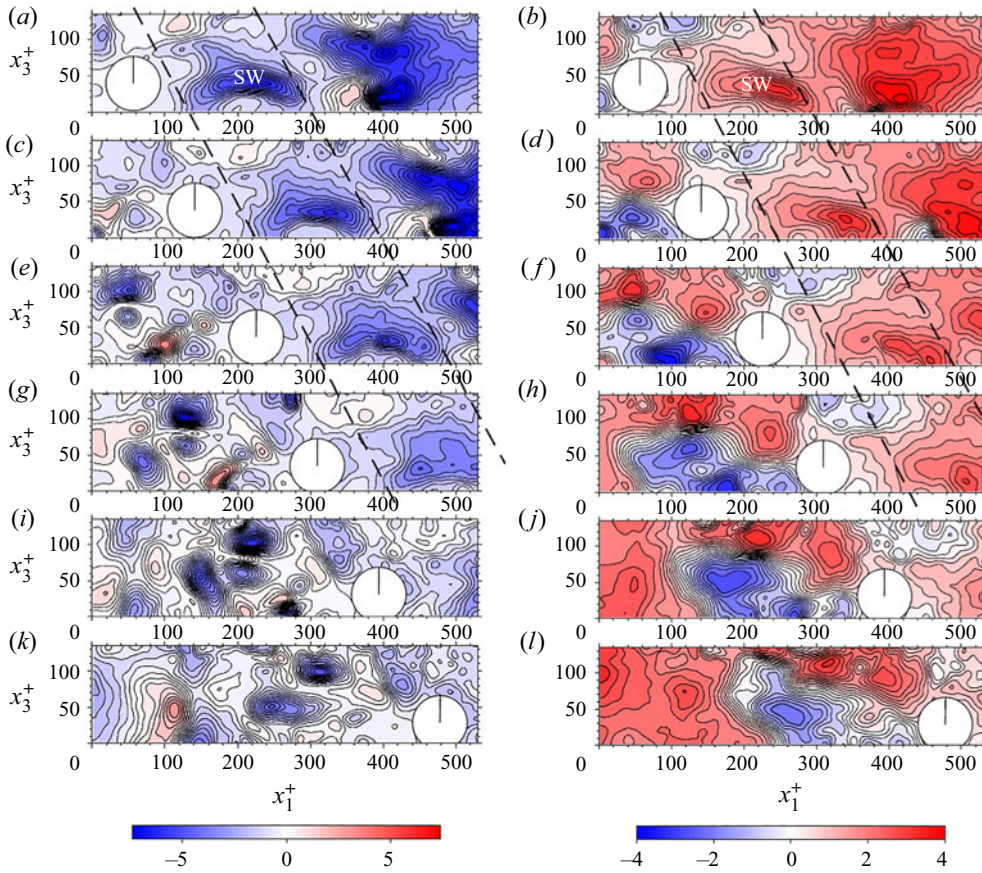
Figure 21. For S_4, a sequence ($\Delta t^+ = 4.9$) of equatorial wall-parallel planes depicting the correlations of the instantaneous water fluctuating velocities $(u_1 u_2)^+$ (a,c,e,g,i,k), and the streamwise water fluctuating velocities u_1^+ (b,d,f,h,j,l). The hydrogel sphere is superposed as a filled white circle. Its initial orientation is indicated by a dashed line, while its changing orientation is indicated by a solid line. A progressing sweep motion (SW) can be seen between the two parallel dashed lines in (a–h). Note that the view is from the wall upwards.

shear-induced lift force has been a topic of investigation for many decades (see Zeng *et al.* 2009; Shi & Rzehak 2019, 2020). Correlations valid for extended ranges of Re_s and shear rate magnitude have been proposed (see recent reviews by Shi & Rzehak 2019, 2020).

In analogy with the drag force (3.1), the shear-induced lift force acting on the sphere can be determined by

$$F_L^S = C_L^S \rho \, \frac{\pi}{8} \, D^2 \, |U_r|^2 \, e_{\perp \Omega}, \tag{3.3}$$

where C_L^S denotes the shear-induced lift coefficient (indicated by the superscript 'S'), and $e_{\perp \Omega}$ is the unit vector in the direction of ($\Omega \times U_r$), where '$\times$' denotes the cross product. An expression similar to (3.3) may be used for the wall-induced lift (superscript 'W'), albeit with a different lift coefficient, C_L^W (Shi & Rzehak 2020). In addition to the shear and wall-induced lift forces, the Magnus force (based on inviscid flow analysis) can be determined by

$$F_L^R = C_L^R \rho \, \frac{\pi}{8} \, D^2 \, |U_r|^2 \, e_{\perp \dot\alpha}, \tag{3.4}$$

944 A12-29

where C_L^R denotes the rotation-induced lift coefficient (denoted by the superscript 'R'), and $\boldsymbol{e}_{\perp\dot{\alpha}}$ is the unit vector in the direction of ($\dot{\boldsymbol{\alpha}} \times \boldsymbol{U}_r$).

Care must be taken with regard to the sign of the lift forces since it depends on whether viscous or inviscid lift mechanisms dominate. The direction of the Magnus force (inviscid case) is always towards the advancing side of the sphere. However, with viscous effects taken into account, boundary layer growth and separation may be different along the advancing and retreating sphere surfaces, thereby reversing the direction of the Magnus force (the so-called 'inverse' Magnus effect; Kim *et al.* 2014). As outlined by Kim *et al.* (2014), the inverse Magnus effect occurs at high Reynolds numbers ($\sim 10^5$) and is not expected to play a role here.

As seen in (3.3), the direction of $\boldsymbol{F}_L^S$ is perpendicular to ($\boldsymbol{\Omega} \times \boldsymbol{U}_r$), which means that in a wall-bounded linear shear flow, it depends on the sign of U_r (Shi & Rzehak 2020), i.e. F_L^S may be either positive (directed away from the wall when $U_r < 0$) or negative (directed towards the wall when $U_r > 0$). Also, the wall-induced lift force may be directed towards or away from the wall depending on the relative dominance of viscous or inviscid lift mechanisms (see Zeng *et al.* 2009). Furthermore, DNS studies showed that the sign of F_L^S is a function of Re_s (Kurose & Komori 1999; Zeng *et al.* 2009; Shi & Rzehak 2019), i.e. when $Re_s > 55$ flow separation resulted in asymmetrical distributions of pressure and viscous stresses, and the lift force became negative (see also Kurose & Komori 1999; Zeng *et al.* 2009; Shi & Rzehak 2019). Negative lift has also been observed in the vicinity of a wall and is strongest when the sphere is located about one diameter from it (Zeng *et al.* 2009).

Based on DNS studies, a correlation for the shear-induced lift coefficient for a stationary sphere in a wall-bounded linear shear flow has been proposed by Zeng *et al.* (2009):

$$C_L^S = C_{L,w}^S \exp(-0.5\delta(Re_s/250)^{4/3}) \left[\exp(\alpha_L^S \delta^{\beta_L^S}) - \lambda_L^S \right], \tag{3.5}$$

where $\alpha_L^S = -\exp(-0.3 + 0.025Re_s)$, $\beta_L^S = 0.8 + 0.01Re_s$, and $\lambda_L^S = (1 - \exp(-\delta))$ $(Re_s/250)^{5/2}$; here, $C_{L,w}^S = 3.663/(Re_s^2 + 0.1173)^{0.22}$ denotes the lift coefficient in the limit of the sphere touching the wall (denoted by the subscript 'w'). Equation (3.5) is valid in the range $1 < Re_s < 200$. Note that the correlation for C_L^S (3.5) does also include the effect of wall proximity, which reduces with increasing δ (see Zeng *et al.* 2009). Therefore, in the present case, values of C_L^S according to (3.5) are enhanced over their unbounded counterparts. A correlation for the wall-induced lift coefficient on a sphere moving parallel to a wall in a quiescent fluid is given by (Zeng *et al.* 2009)

$$C_L^W = f + \left[C_{L,w}^W - f_{x_{2,c}/D=1/2} \right] \exp\left[-11(\delta/\delta_c)^{1.2} \right], \tag{3.6}$$

where $\delta_c = 3\exp(-0.17Re_s^{0.7})$, and $f(x_{2,c}/D, Re_s) = (1 + 0.329Re_s + 0.00485Re_s^2)$ $C_{L,w}^W(x_{2,c}/D)^{[-0.9\tanh(0.022Re_s)]}$. The wall-induced lift coefficient for a sphere touching the wall is given by $C_{L,w}^W = (9/8 + 5.78 \times 10^{-6}(Re_s\,x_{2,c}/D)^{4.58})\exp(-0.292Re_s\,x_{2,c}/D)$ for $0 < Re_s\,x_{2,c}/D < 10$, and $C_{L,w}^W = 8.94(Re_s\,x_{2,c}/D)^{-2.09}$ for $10 < Re_s\,x_{2,c}/D < 300$ (Takemura & Magnaudet 2003). Finally, a correlation for the rotation-induced lift coefficient was adopted from Bagchi & Balachandar (2002):

$$C_{L,i}^R \approx -0.55\dot{\alpha}_3 D/|U_r|. \tag{3.7}$$

Note that only the correlation for C_L^S (see (3.5)) takes flow separation into account, and the sign of C_L^S may be reversed (negative lift) depending on Re_s.

944 A12-30

The additive nature of the different contributions to the lift force has been investigated by Bagchi & Balachandar (2002), Zeng (2007) and Bluemink *et al.* (2008). Zeng (2007) showed that linear superposition of wall and shear contributions is incorrect and underestimates the actual lift coefficient especially when close to the wall ($2x_{2c}/D \leq 2$; Shi *et al.* 2021) and for low Re_s ($1 \leq Re_s \leq 100$; see also Shi *et al.* 2021). However, combined wall and shear contributions (superimposed nonlinearly) do superimpose linearly with the rotational contribution to the total lift coefficient (Shi *et al.* 2021), in agreement with Bagchi & Balachandar (2002) and Bluemink *et al.* (2008), who concluded that the total lift force on a freely rotating sphere in a shear flow ($0 < Re_s \leq 200$) can be taken as the superposition of the lift on a stationary sphere in a shear flow (3.3) and the lift on a sphere forced to spin at the torque-free rotation rate in a uniform flow. As shown by Bagchi & Balachandar (2003), freestream turbulence did not have a substantial effect on the time-averaged drag that could be determined accurately by the standard drag relation. However, accurate prediction of the instantaneous drag deteriorated with increasing particle size. Once vortex shedding occurred for $Re_s > 270$ (Bagchi & Balachandar 2003), the effect of isotropic freestream turbulence on the lift forces appeared to be minor. Note that the effect of non-isotropic ambient turbulence such as in a TBL has not been studied (see Shi & Rzehak 2020), and it is unclear if the available correlations are valid for spheres immersed in a TBL. Therefore, magnitudes of the drag and lift forces calculated here must be interpreted with caution.

In the absence of gravitation, the lift and drag forces are expected to be important for sphere motion in the transverse plane, where especially S_1 and S_3 exhibit strong transverse motion in opposite directions (figure 8b). The instantaneous transverse components of F_L^R, F_L^S, F_L^W and F_D calculated by (3.1)–(3.7), and normalized by $\rho \nu^2$, are depicted in figure 22 for all four spheres. Note that the instantaneous drag forces based on C_D (see (3.2); open symbols in figures 22d and 23d) are compared to those based on the standard drag relation (filled symbols in figures 22d and 23d). Overall, trends are conserved, and besides some discrepancies at peak values (figure 22d), differences are relatively small. In the following, values of C_D (see (3.2)) were used. Average and r.m.s. values of the forces along the spheres' tracks are summarized in table 6. Comparing figures 22(b,c), it can be observed that the instantaneous values of $F_{L,3}^{S+}$ and $F_{L,3}^{W+}$ change in tandem, albeit with smaller magnitudes for $F_{L,3}^{W+}$ (similarly in the wall-normal direction; figures 23b,c). In all cases, magnitudes of the shear-induced and wall-induced forces are small in comparison to those of the drag force (see also table 6). In contrast, the magnitudes of the average rotation-induced lift force (table 6) exceed those of the shear- and wall-induced lift forces in all cases. Note that in many cases, values of $|\overline{F_{L,2}^{R+}}|$ are of the same order of magnitude as $|\overline{F_{D,i}^+}|$ (table 6).

Let us now first focus on spheres S_1 and S_3 that move in opposite transverse directions. It can be observed that the peak magnitudes of the instantaneous transverse drag force components acting on S_1 and S_3 (figure 22d) are much larger than those of the corresponding lift forces (figures 22a–c) that do not seem to play a role. Although the instantaneous drag force fluctuates along the S_1 trajectory (figure 22d), $|\overline{F_{D,3}^+}|$ (table 6) is much larger than the corresponding magnitudes of the average lift forces, and is directed in the direction of its motion (see figure 8). In contrast to S_1, for S_3 the average contributions to the total lift force have higher magnitudes and taken together are of the same order of magnitude as the average drag force (see table 6). Note that linear superposition of
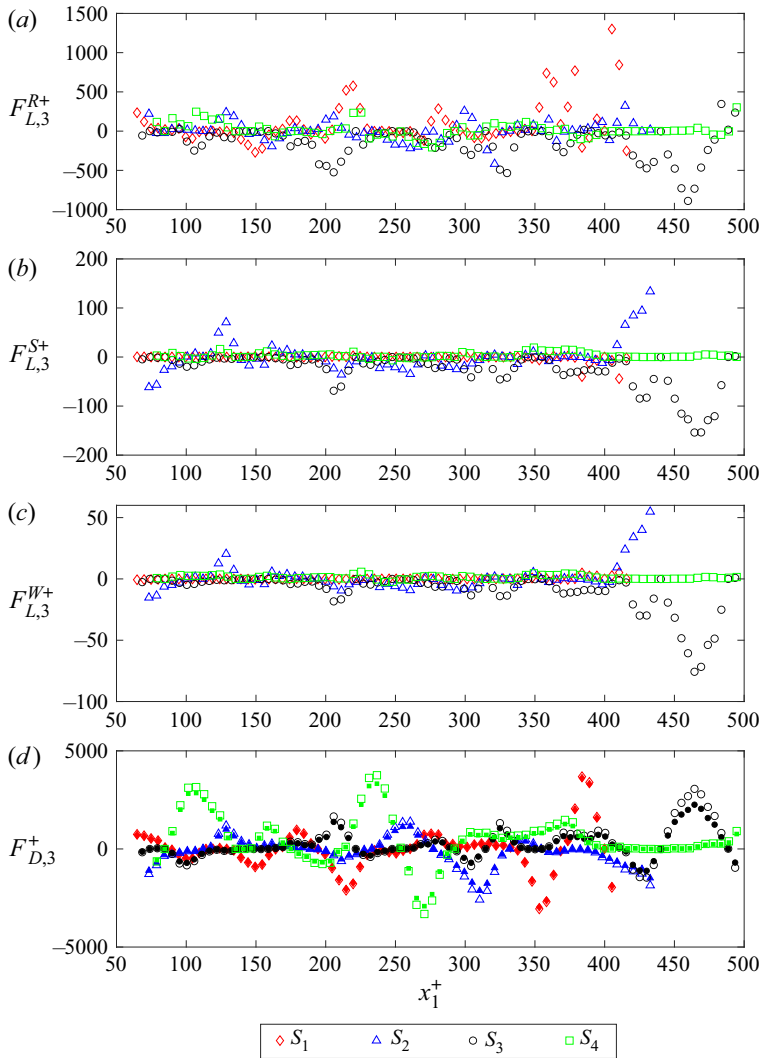
Figure 22. The instantaneous normalized transverse components of (*a*) the Magnus force, (*b*) the shear-induced lift force, (*c*) the wall-induced lift force, and (*c*) the drag force, acting on the spheres. Solid symbols in (*d*) denote values according to the standard drag relation. Note that the *y*-axis ranges are different.

the wall- and shear-induced lift contribution is expected to underestimate the actual total lift force (Shi *et al.* 2021). Surprisingly, the average lift forces oppose the S_3 motion (see figure 8). Similarly, for S_2 and S_4, on average, the transverse lift force components oppose the spheres' motion in the x_3-direction. However, in these cases, lift forces are at least one order of magnitude lower than the drag and do not seem to play a role.

The present results may indicate that the sign of the lift coefficient is incorrect and that viscous effects play a role. Evidence that negative lift may be important is provided by looking at the transverse equatorial planes of u_1^+ depicted in figures 17*b*,*d*,*f*,*h* for S_3. It is clear that S_3 moves in the positive x_3-direction towards the low streamwise velocity side, hinting that negative lift due to viscous effects such as flow separation might be important. Note that for S_3, most Re_s values were below 55 (figure 11), and using (3.5) did not result in negative lift, suggesting that the relation (3.5) for C_L^S may need to be modified in the

	i	$\overline{F_{L,i}^{S+}}$	$(F_{L,i}^{S+})'$	$\overline{F_{L,i}^{W+}}$	$(F_{L,i}^{W+})'$	$\overline{F_{L,i}^{R+}}$	$(F_{L,i}^{R+})'$	$\overline{F_{D,i}^{+}}$	$(F_{D,i}^{+})'$
S_1	1	3.73	3.2	−1.42	0.82	−227.3	167.9	446.4	294.4
	2	−4.93	6.4	2.03	1.5	361.0	294.4	1266.6	548.7
	3	−1.58	7.3	0.21	1.0	86.6	268.6	−545.2	3206.0
S_2	1	−14.4	36.0	−5.6	14.0	−30.8	124.5	94.0	700.8
	2	4.8	15.9	1.66	4.8	15.1	104.6	71.6	231.0
	3	0.69	31.6	0.86	11.4	4.1	126.0	−193.9	784.9
S_3	1	20.2	25.8	6.8	8.6	141.3	202.4	534.2	314.6
	2	13.6	21.0	4.9	7.6	82.8	130.2	−70.3	209.5
	3	−26.3	36.5	−9.9	16.0	−153.1	206.8	282.1	853.7
S_4	1	−2.5	7.0	−0.63	2.0	−26.0	50.7	95.5	194.6
	2	2.4	6.2	0.73	1.8	17.6	61.1	77.4	120.7
	3	3.4	5.2	1.3	1.6	16.2	91.3	508.8	1267.6

Table 6. Summary of the average and r.m.s. values of the components of the shear-induced, wall-induced and Magnus lift forces, as well as the drag forces acting on the spheres along their trajectories.

case of a sphere immersed in a TBL. Unfortunately, and despite considerable effort, we could not validate that flow separation occurred, nor did we observe vortex shedding from the sphere. However, at these relatively low Re_s values, it would be difficult to detect flow separation since the wake length is small (increasing linearly from $0.2D$ at $Re_s \approx 30$ to $1D$ at $Re_s \approx 100$; Taneda 1956), and the surrounding turbulence together with the limited spatial measurement resolution would act to smear any signs of it.

The wall-normal trajectories of the spheres depicted in figure 8(*a*) show that except for S_1, which remains more or less at the same height, all other spheres move towards the wall. The normalized instantaneous wall-normal components of F_L^{R+}, F_L^{S+}, F_L^{W+} and F_D^{+} are plotted in figure 23 for all four spheres, and average values are summarized in table 6. In the case of S_1, the wall-normal shear- and wall-induced lift forces (figures 23*b,c*) do not play a role, and the drag force aided by the rotation-induced lift force (figures 23*a,d*) acting away from the wall keeps S_1 aloft. In most cases, the magnitude of the average rotation-induced lift force (table 6) that always acts away from the wall is of the same order of magnitude as the average wall-normal drag force component. Note that only for S_3 does the average drag force aid wall-ward motion, while in all other cases it opposes it. While the shear- and wall-induced lift forces cannot be superimposed linearly (Shi *et al.* 2021), their average values are small and they do not seem to be important. While the instantaneous lift forces fluctuate along the spheres' trajectories (figures 23*a–c*), for S_3 they are directed consistently away from the wall, i.e. opposing the S_3 wall-ward motion. Moreover, also for S_2 and S_4, the different contributions to the average lift force and $\overline{F_D^{+}}$ (table 6) are directed away from the wall, which would explain why all wall-ward moving spheres have wall-normal velocity magnitudes lower than $|V_s|$. Note that of the lift forces, $\overline{F_{L,i}^{R+}}$ cannot be neglected, and magnitudes of $\overline{F_{L,i}^{R+}}$ can be of the same order of magnitude as the drag (table 6).

In the streamwise direction, it can be observed that components of the lift forces in addition to those of the drag forces play a role (see table 6), either acting in the direction of the sphere's motion or opposing it. In all cases, the average drag force is positive ($\overline{F_{D,1}^{+}} > 0$; table 6), since on average, all spheres lag the streamwise water velocity (table 1).
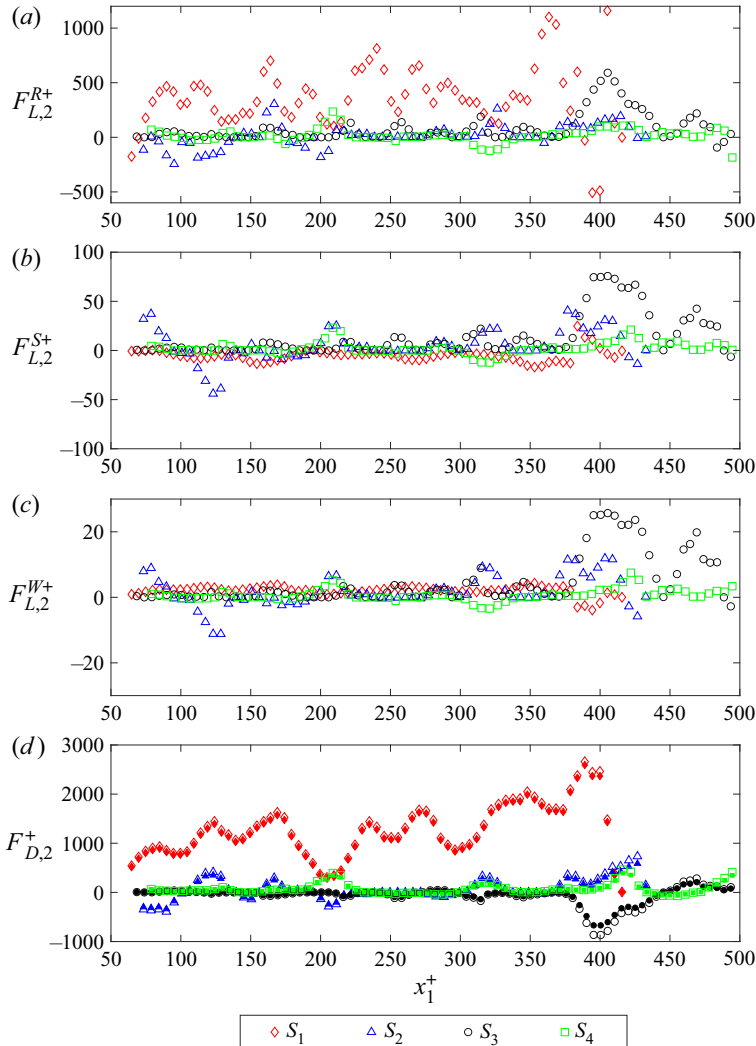
Figure 23. The instantaneous, normalized wall-normal components of (*a*) the Magnus lift force, (*b*) the shear-induced lift force, (*c*) the wall-induced lift force, and (*d*) the drag force, acting on the spheres. The solid symbols in (*d*) denote values according to the standard drag relation. Note that the *y*-axis ranges are different.

Since the instantaneous sphere velocities exhibit fluctuations along their tracks (see § 3.2.1), inertial forces may be of importance. However, their accurate evaluation is non-trivial. The commonly used force balance derived by Maxey & Riley (1983) is strictly valid only when the ratio between the sphere diameter and the Kolmogorov length scale, D/η_k, is smaller than unity, which is not the case in the present study. Nevertheless, since we do not resolve the boundary layer close to the sphere's surface, the expressions provided by Maxey & Riley (1983) were used to estimate the order of magnitude of the inertial forces. Results (not shown) indicated that normalized inertial forces averaged along the sphere tracks (fluid pressure and added mass forces) mostly had an order of magnitude of 10^3, i.e. the same order of magnitude as that of the inertial force associated with sphere acceleration. The inertial forces are expected to 'cancel' each other such that their net effect would be of the same order of magnitude as the other forces acting on the sphere

944 A12-34

(such as drag and lift). However, this could not be validated due to the large uncertainties associated with the estimates of the inertial terms.

In addition, the Basset history force may play a role (Dorgan & Loth 2007; Calzavarini *et al.* 2012). Estimating it based on a force balance similarly as done by Takemura & Magnaudet (2003) was not deemed feasible since estimates of the inertial forces were not accurate enough (as outlined above). However, we do not believe that the history force is significant in the current measurements, for the following reasons. The transport of the vorticity generated at the sphere's surface away from it can be characterized by several time scales. The first is associated with initial viscous diffusion of the vorticity generated at the sphere's surface across the Stokes layer ($\nu/|U_r| \approx 0.1$ mm; Zeng *et al.* 2009) given by $\nu/|U_r|^2 \approx 10$ ms, which is comparable to the Kolmogorov time scale of the surrounding turbulence (see table 3). Beyond the Stokes layer, advection will govern, which is characterized by a time scale given by $D/|U_r| \sim 1$ s. This advective time scale is much larger (more than two orders of magnitude) than the smallest turbulence time scales (see table 3) in the present study. Therefore, the 'memory' effect of the Basset history force is expected to be quickly 'smeared out' by the action of the surrounding turbulence (turbulent diffusion).

4. Summary and conclusions

The interaction between freely moving, nearly neutrally buoyant spheres ($66 \leq D^+ \leq 75$) and a TBL was investigated by a combination of PIV, refractive index matching and computer vision algorithms. Experiments were conducted in a turbulent open water channel flow, and in order to track the rotational and translational motion of refractive index matched hydrogel spheres, they were 'tagged' by tracer particles inserted as 'spokes'. The 3-D flow field in their vicinity was measured using time-resolved tomo-PIV.

A method for extracting the spheres' 3-D motion (translation and rotation) and the surrounding 3-D flow field was developed. First, the sphere's perimeter was detected at each time instant in each of the four simultaneously acquired 2-D PIV images using the circular Hough transform. Subsequently, based on the detected sphere silhouettes, the sphere's visual hull was reconstructed at each time instant (Adhikari & Longmire 2012), and its diameter and instantaneous centroid position were estimated and used to mask the instantaneous 3-D reconstructed light intensity distributions. The sphere's motion was tracked across frames using the iterative closest point (ICP) algorithm. The 3-D flow field in the vicinity of the sphere was determined using standard tomo-PIV data processing techniques.

Of the four investigated spheres, three (S_2, S_3 and S_4) moved towards the wall, while one (S_1) remained at approximately the same height. None of the spheres came into contact with the wall, and due to their finite size, they were positioned within the buffer and the log layer of the TBL. The wall-ward moving spheres were located just upstream of strong sweep motions induced by the surrounding coherent structures. In the case of S_1, the wall-normal drag force component was directed consistently away from the wall, and together with the rotation-induced lift force, it was responsible for keeping the sphere aloft. Shear- and wall-induced lift forces did not play a role in any of the cases. However, the magnitude of the mean rotation-induced lift force was in most cases of the same order of magnitude as that of the drag force.

In the transverse direction, gravity did not play a role, and lift and drag forces were expected to be of importance. While the (average) transverse drag force component was always important (both aiding as well as opposing the transverse sphere motion), lift

forces were small compared to the drag force. The only exception was S_3, for which the transverse lift forces were of the same order of magnitude as the transverse drag force component. However, in this case the lift forces acting on the spheres were directed towards the fast-moving fluid, in agreement with inviscid lift mechanisms, while S_3 moved in the opposite direction, i.e. towards the slow-moving fluid. This puzzling result might indicate that viscous effects (e.g. flow separation) that are not accounted for at these Re_s values in the employed correlations ((3.2) and (3.5)–(3.7)) may play a role and lead to negative lift. Note that the correlations do not account for the effect of non-homogeneous ambient turbulence as in the case of a TBL. Unfortunately, due to spatial resolution limitations and the surrounding turbulence, signs of flow separation (such as a recirculating wake) were not detected.

Estimated orders of magnitude of inertial forces such as the fluid pressure and the added mass force exceeded those of the drag force. However, their net effect should balance the other forces acting on the sphere. The Basset history force was not considered of importance in the present study as its 'memory' effect is expected to be quickly 'erased' by the ambient turbulence.

The instantaneous vortices in the TBL in the vicinity of two spheres (S_3 and S_4) were analysed in detail. In both cases, the spheres moved towards the wall and were positioned just upstream of strong distinct sweep motions. In addition, upstream of S_4, a large hairpin packet was observed whose development was affected by the downward motion of the sphere. Evidence for this was provided by the observation that S_4 was positioned on top of a hairpin vortex that looked to be part of the upstream hairpin packet, which was distorted due to the presence of S_4. Note that the finite size of the spheres ($D^+ \approx 70$) is approximately half of commonly encountered transverse extents of hairpin vortices ($\Delta x_2^+ \approx 150$). Ultimately, at increased volume fractions, these finite-size effects are expected to affect drastically the structure of the near-wall coherent structures in TBLs, with implications for wall friction, heat and momentum transfer.

The present measurements have provided novel, detailed information on the coupling between the instantaneous 3-D flow field and sphere dynamics for finite-sized spheres in a fully developed TBL. In the coming decades, these advanced measurements are expected to bridge the existing knowledge gap on the coupling between turbulent flows and finite-size particles in particle-laden flows. Future research should focus on the acquisition of increased statistics in order to extend and validate the present findings, as well as on the development and validation of correlations for lift coefficients that can be applied to finite-sized particles in TBL flows.

Author ORCIDs.
 R. van Hout https://orcid.org/0000-0002-4042-7936;
 G.E. Elsinga https://orcid.org/0000-0001-6717-5284.

REFERENCES

ADHIKARI, D. & LONGMIRE, E.K. 2012 Visual hull method for tomographic PIV measurement of flow around moving objects. *Exp. Fluids* **53** (4), 943–964.

ADRIAN, R.J. 2007 Hairpin vortex organization in wall turbulence. *Phys. Fluids* **19** (4), 041301.

ADRIAN, R.J. 2011 *Particle Image Velocimetry*. Cambridge University Press.

AHMADI, F., SANDERS, S. & GHAEMI, S. 2020 Experimental investigation of three-dimensional flow around particles in a turbulent channel flow. *Phys. Rev. Fluids* **5** (1), 014302.

ARDEKANI, M.N. & BRANDT, L. 2019 Turbulence modulation in channel flow of finite-size spheroidal particles. *J. Fluid Mech.* **859**, 887–901.

BAGCHI, P. & BALACHANDAR, S. 2002 Effect of free rotation on the motion of a solid sphere in linear shear flow at moderate *Re*. *Phys. Fluids* **14** (8), 2719–2737.

BAGCHI, P. & BALACHANDAR, S. 2003 Effect of turbulence on the drag and lift of a particle. *Phys. Fluids* **15** (11), 3496–3513.

BAGNOLD, R.A. 1951 The movement of a cohesionless granular bed by fluid flow over it. *Brit. J. Appl. Phys.* **2** (2), 29–34.

BAKER, L.J. & COLETTI, F. 2021 Particle–fluid–wall interaction of inertial spherical particles in a turbulent boundary layer. *J. Fluid Mech.* **908**, A34.

BALACHANDAR, S. & EATON, J.K. 2010 Dispersed turbulent multiphase flow. *Annu. Rev. Fluid Mech.* **42**, 111–133.

BELLANI, G., BYRON, M.L., COLLIGNON, A.G., MEYER, C.R. & VARIANO, E.A. 2012 Shape effects on turbulent modulation by large nearly neutrally buoyant particles. *J. Fluid Mech.* **712**, 41–60.

BLUEMINK, J.J., LOHSE, D., PROSPERETTI, A. & VAN WIJNGAARDEN, L. 2008 A sphere in a uniformly rotating or shearing flow. *J. Fluid Mech.* **600**, 201–233.

BRETHERTON, F.P. 1962 The motion of rigid particles in a shear flow at low Reynolds number. *J. Fluid Mech.* **14** (2), 284–304.

CALZAVARINI, E., VOLK, R., LÉVÊQUE, E., PINTON, J.-F. & TOSCHI, F. 2012 Impact of trailing wake drag on the statistical properties and dynamics of finite-sized particle in turbulence. *Physica* D **241** (3), 237–244.

CLAUSER, F.H. 1956 The turbulent boundary layer. *Advances in Applied Mechanics*, **4**, 1–51.

CLEVELAND, W.S. 1979 Robust locally weighted regression and smoothing scatterplots. *J. Am. Stat. Assoc.* **74** (368), 829–836.

CLIFT, R., GRACE, J.R. & WEBER, M.E. 1978 *Bubbles, Drops, and Particles*. Academic Press California.

DALITZ, C., SCHRAMKE, T. & JELTSCH, M. 2017 Iterative Hough transform for line detection in 3D point clouds. *Image Process. On Line* **7**, 184–196.

DE GRAAFF, D.B. & EATON, J.K. 2000 Reynolds-number scaling of the flat-plate turbulent boundary layer. *J. Fluid Mech.* **422**, 319–346.

DORGAN, A.J. & LOTH, E. 2007 Efficient calculation of the history force at finite Reynolds numbers. *Intl J. Multiphase Flow* **33** (8), 833–848.

EBRAHIMIAN, M., SANDERS, S.R. & GHAEMI, S. 2019 Dynamics and wall collision of inertial particles in a solid–liquid turbulent channel flow. *J. Fluid Mech.* **881**, 872–905.

ELSINGA, G.E., ADRIAN, R.J., VAN OUDHEUSDEN, B.W. & SCARANO, F. 2010 Three-dimensional vortex organization in a high-Reynolds-number supersonic turbulent boundary layer. *J. Fluid Mech.* **644**, 35–60.

ELSINGA, G.E., SCARANO, F., WIENEKE, B. & VAN OUDHEUSDEN, B.W. 2006 Tomographic particle image velocimetry. *Exp. Fluids* **41** (6), 933–947.

ELSINGA, G.E. & WESTERWEEL, J. 2011 Tomographic-PIV measurement of the flow around a zigzag boundary layer trip. *Exp. Fluids* **52** (4), 865–876.

ERM, L.P. & JOUBERT, P.N. 1991 Low-Reynolds-number turbulent boundary layers. *J. Fluid Mech.* **230**, 1–44.

GARCIA, D. 2010 Robust smoothing of gridded data in one and higher dimensions with missing values. *Comput. Stat. Data Anal.* **54** (4), 1167–1178.

VAN HOUT, R. 2011 Time-resolved PIV measurements of the interaction of polystyrene beads with near-wall-coherent structures in a turbulent channel flow. *Intl J. Multiphase Flow* **37** (4), 346–357.

VAN HOUT, R. 2013 Spatially and temporally resolved measurements of bead resuspension and saltation in a turbulent water channel flow. *J. Fluid Mech.* **715**, 389–423.

VAN HOUT, R., EISMA, J., ELSINGA, G.E. & WESTERWEEL, J. 2018 Experimental study of the flow in the wake of a stationary sphere immersed in a turbulent boundary layer. *Phys. Rev. Fluids* **3** (2), 024601.

VAN HOUT, R., SABBAN, L. & COHEN, A. 2013 The use of high-speed PIV and holographic cinematography in the study of fiber suspension flows. *Acta Mech.* **224** (10), 2263–2280.

HUNT, J.C.R., WRAY, A.A. & MOIN, P. 1988 Eddies, streams, and convergence zones in turbulent flows. In *Proceedings of the 1988 Summer Program of the Center for Turbulence Research*, pp. 193–208. NASA Ames/Stanford University.

KANE, I.A. & CLARE, M.A. 2019 Dispersion, accumulation, and the ultimate fate of microplastics in deep-marine environments: a review and future directions. *Front. Earth Sci.* **7**, 80.

KIM, J., CHOI, H., PARK, H. & YOO, J.Y. 2014 Inverse Magnus effect on a rotating sphere: when and why. *J. Fluid Mech.* **754**, R2.

KLEIN, S., GIBERT, M., BÉRUT, A. & BODENSCHATZ, E. 2012 Simultaneous 3D measurement of the translation and rotation of finite-size particles and the flow field in a fully developed turbulent water flow. *Meas. Sci. Technol.* **24** (2), 024006.

KUROSE, R. & KOMORI, S. 1999 Drag and lift forces on a rotating sphere in a linear shear flow. *J. Fluid Mech.* **384**, 183–206.

MAXEY, M.R. & RILEY, J.J. 1983 Equation of motion for a small rigid sphere in a nonuniform flow. *Phys. Fluids* **26** (4), 883–889.

MINIER, J.-P. & POZORSKI, J. 2017 *Particles in Wall-Bounded Turbulent Flows: Deposition, Re-suspension and Agglomeration*. Springer.

MOLLINGER, A.M. & NIEUWSTADT, F.T.M. 1996 Measurement of the lift force on a particle fixed to the wall in the viscous sublayer of a fully developed turbulent boundary layer. *J. Fluid Mech.* **316**, 285–306.

MUTHANNA, C., NIEUWSTADT, F.T.M. & HUNT, J.C.R. 2005 Measurement of the aerodynamic forces on a small particle attached to a wall. *Exp. Fluids* **39** (2), 455–463.

NIÑO, Y. & GARCIA, M.H. 1996 Experiments on particle–turbulence interactions in the near-wall region of an open channel flow: implications for sediment transport. *J. Fluid Mech.* **326**, 285–319.

PEDERSEN, S.J.K. 2007 Circular Hough transform. *Aalborg Univ. Vision Graph. Interact. Syst.* **123** (6).

PENG, C., AYALA, O.M. & WANG, L.-P. 2019 A direct numerical investigation of two-way interactions in a particle-laden turbulent channel flow. *J. Fluid Mech.* **875**, 1096–1144.

POPE, S.B. 2000 *Turbulent Flows*. Cambridge University Press.

RABENCOV, B., ARCA, J. & VAN HOUT, R. 2014 Measurement of polystyrene beads suspended in a turbulent square channel flow: spatial distributions of velocity and number density. *Intl J. Multiphase Flow* **62**, 110–122.

RABENCOV, B. & VAN HOUT, R. 2015 Voronoi analysis of beads suspended in a turbulent square channel flow. *Intl J. Multiphase Flow* **68**, 10–13.

RASHIDI, M., HETSRONI, G. & BANERJEE, S. 1990 Particle–turbulence interaction in a boundary layer. *Intl J. Multiphase Flow* **16** (6), 935–949.

ROBINSON, S.K. 1991 Coherent motions in the turbulent boundary layer. *Annu. Rev. Fluid Mech.* **23** (1), 601–639.

SAFFMAN, P.G.T. 1965 The lift on a small sphere in a slow shear flow. *J. Fluid Mech.* **22** (2), 385–400.

SAKAMOTO, H. & HANIU, H. 1990 A study on vortex shedding from spheres in a uniform flow. *Trans. ASME J. Fluids Engng* **112**, 386–392.

SCHLICHTING, H. & GERSTEN, K. 2000 *Boundary-Layer Theory*. Springer.

SEGRE, G. & SILBERBERG, A. 1962 Behaviour of macroscopic rigid spheres in Poiseuille flow. Part 2. Experimental results and interpretation. *J. Fluid Mech.* **14** (1), 136–157.

SHI, P. & RZEHAK, R. 2019 Lift forces on solid spherical particles in unbounded flows. *Chem. Engng Sci.* **208**, 115145.

SHI, P. & RZEHAK, R. 2020 Lift forces on solid spherical particles in wall-bounded flows. *Chem. Engng Sci.* **211**, 115264.

SHI, P., RZEHAK, R., LUCAS, D. & MAGNAUDET, J. 2021 Drag and lift forces on a rigid sphere immersed in a wall-bounded linear shear flow. *Phys. Rev. Fluids* **6** (10), 104309.

SMISTAD, E., FALCH, T.L., BOZORGI, M., ELSTER, A.C. & LINDSETH, F. 2015 Medical image segmentation on GPUs – a comprehensive review. *Med. Image Anal.* **20** (1), 1–18.

SOLDATI, A. & MARCHIOLI, C. 2009 Physics and modelling of turbulent particle deposition and entrainment: review of a systematic study. *Intl J. Multiphase Flow* **35** (9), 827–839.

SUMER, B.M. & DEIGAARD, R. 1981 Particle motions near the bottom in turbulent flow in an open channel. Part 2. *J. Fluid Mech.* **109**, 311–337.

SUMER, B.M. & OGUZ, B. 1978 Particle motions near the bottom in turbulent flow in an open channel. *J. Fluid Mech.* **86** (1), 109–127.

SUTHERLAND, A.J. 1967 Proposed mechanism for sediment entrainment by turbulent flows. *J. Geophys. Res.* **72** (24), 6183–6194.

TAKEMURA, F. & MAGNAUDET, J. 2003 The transverse force on clean and contaminated bubbles rising near a vertical wall at moderate Reynolds number. *J. Fluid Mech.* **495**, 235–253.

TANEDA, S. 1956 Experimental investigation of the wake behind a sphere at low Reynolds numbers. *J. Phys. Soc. Japan* **11** (10), 1104–1108.

TEE, Y.H., BARROS, D.C. & LONGMIRE, E.K. 2020 Motion of finite-size spheres released in a turbulent boundary layer. *Intl J. Multiphase Flow* **133**, 103462.

WIENEKE, B. 2008 Volume self-calibration for 3D particle image velocimetry. *Exp. Fluids* **45** (4), 549–556.

WOODCOCK, C.R. & MASON, J.S. 1987 *Hydraulic Conveying*, pp. 478–493. Springer Netherlands.

YAM, K., BURNS, A.D., INGHAM, D.B. & McCAFFREY, W.D. 2013 Influence of lift force on the settling velocities of rotating particles in two-dimensional shear flow. *ASCE J. Hydraul. Engng* **139** (12), 1277–1285.

YOUSEFI, A., COSTA, P. & BRANDT, L. 2020 Single sediment dynamics in turbulent flow over a porous bed – insights from interface-resolved simulations. *J. Fluid Mech.* **893**, A24.

ZENG, L. 2007 *Interaction between a spherical particle and wall-bounded flows at finite Reynolds number*. PhD Dissertation, theoretical and Apllied Mechanics in the Graduate College of the University of Illinois at Urbana-Champaign.

ZENG, L., NAJJAR, F., BALACHANDAR, S. & FISCHER, P. 2009 Forces on a finite-sized particle located close to a wall in a linear shear flow. *Phys. Fluids* **21** (3), 033302.

ZHAO, L. & ANDERSSON, H.I. 2011 On particle spin in two-way coupled turbulent channel flow simulations. *Phys. Fluids* **23** (9), 093302.